A Novel Imaging Mass Spectrometry Computational Tool for Biomedical Discovery: Untargeted pixel-by-pixel imaging of Metabolite Ratio Pairs

Huiyong Cheng[1], Dawson Miller[1], Nneka Southwell[5], Joshua L. Fischer[2], J. Michael Salbaum[3], Claudia Kappen[3], Fenghua Hu[4], Cha Yang[4], Steven S. Gross[1], Marilena D'Aurelio[5], and Qiuying Chen[1*]

[1]Department of Pharmacology and Brain and Mind Research Institute[5],Weill Cornell Medicine, New York, NY 10021

[2]Bruker Daltonics, Billerica, MA 01821

[3]Pennington Biomedical Research Center, Louisiana State University, Baton Rouge, LA 70808

[4]Cornell University, Department of Molecular Biology & Genetics, Ithaca, NY 14853-7202

*Correspondence should be addressed to:

Dr. Qiuying Chen, Weill Cornell Medicine, Department of Pharmacology, 1300 York Ave., New York, NY 10065. Phone: 212-746-6216. Email: qic2005@med.cornell.edu

Keywords

Metabolomics, mass spectrometry imaging; matrix-assisted laser desorption ionization mass spectrometry imaging, MALDI-MS, spatial metabolomics, metabolite ratio imaging, spatial metabotyping, tissue segmentation, metabolic pathway analysis

Abstract

Mass spectrometry imaging (MSI) is a powerful technology that can be employed to define the spatial distribution and relative abundance of structurally identified and yet-undefined metabolites across a tissue cryosection. While numerous software packages enable pixel-by-pixel imaging of individual metabolite distributions, the research community lacks a discovery tool that provides spatial imaging of all metabolite abundance ratio pairs. Importantly, the recognition of correlating metabolite pairs offers a strategy to discover unanticipated molecules that contribute to or regulate a shared metabolic pathway, uncover hidden metabolic heterogeneity across cells and tissue subregions, and offers a single timepoint indicator of flux through a particular metabolic pathway of interest. Here, we describe the development and implementation of an untargeted R package workflow for pixel-by-pixel imaging of ratios for all metabolites detected in an MSI experiment. Considering untargeted MSI studies of murine brain and embryogenesis, we demonstrate that ratio imaging offers the opportunity to minimize systematic data variation introduced during sample handling or due to instrument drift, markedly enhances spatial image resolution, and can serve to reveal previously unrecognized tissue regions that are metabotype-distinct. Furthermore, ratio imaging facilitates the discovery of novel regional biomarkers, and can provide anatomical information regarding the spatial distribution of metabolite-linked biochemical pathways. The algorithm described herein is generic and can be applied to any MSI dataset containing spatial information for metabolites, peptides or proteins. Importantly, this software package offers a powerful add-on tool that can significantly enhance knowledge obtained from currently employed spatial metabolite profiling technologies.

Abbreviations

Mass spectrometry imaging (MSI); Fourier transform ion cyclotron resonance mass spectrometry (FT-ICR-MS); Matrix-assisted laser desorption/ionization mass spectrometry imaging (MALDI-MSI); Desorption electrospray ionization (DESI); Cytochrome C oxidase (COX); Knockout (KO); Wildtype (WT); Genome-wide association studies (GWAS); Metabolome-wide association studies (MWAS); Phosphatidylethanolamine (PE); Phosphatidic acid (PA); Lyso-phosphatidylethanolamine (LPE); Lyso-phosphatidic acid (LPA); Cyclic phosphatidic acid (CPA); Regions of interest (ROIs), N-Acetylaspartate (NAA); N-Acetylaspartylglutamate (NAAG); NAAG synthetase (NAAGS); N-Acetyltransferase 8 (NAT8); Fatty acid (FA); Phospholipase A1 (PLA1); Phospholipase A2 (PLA2); Docosahexaenoic acid (DHA); Arachidonic acid (AA); Monounsaturated fatty acid (MUFA); Polyunsaturated fatty acids (PUFA); Fatty acid synthase (FAS); Stearoyl-CoA desaturases (SCD); Glutaminase (GLS); Asparagine synthase (ASNS); AMP deaminase (AMPD); Carnosine synthase (CARNS); Hexose kinase (HK); Glutathione (GSH); Glutathione disulfide (GSSG) Glutathione peroxidase (GPX); Principal component analysis (PCA); Partial least square discriminant analysis (PLS-DA); Receiver operating characteristic curve (ROC) curve; Variable importance in projection (VIP); Hierarchical clustering analysis (HCA); Uniform manifold approximation and projection for dimension Reduction (UMAP)

Introduction

Recent developments in mass spectrometry imaging (MSI) enable spatial mapping of the relative distribution and abundances of proteins, peptides, lipids, small molecule metabolites, drugs and elemental isotopes in heterogenous tissue sections[1] with resolution at, or near, cellular[2]. Hence, MSI has become a promising tool in the era of spatial-omics[3-15], especially at the single cell level[16]. Matrix-assisted laser desorption and ionization (MALDI) and desorption electrospray ionization (DESI) are the dominant modes of ionization for MSI. Regardless of the ionization method and pixel size, all MSI analyses provide pixel-by-pixel relative abundances of all detected charged molecular masses, irrespective of whether their structural identities are known, or unknown. Currently employed MSI data processing tools provide 2D or 3D image data visualization as heatmaps from normalized pixel-by-pixel data of acquired mass spectra[17-20] and image analyses are currently limited to relative abundance data only.

Metabolite ratio imaging has been used in medical MRI spectroscopy imaging to study the distribution of metabolites of interest within a tissue[21]. Targeted serum and urine metabolite ratios have previously been used to assess genome-wide GWAS and MWAS association of metabolic traits, given that metabolite abundance ratios can serve as proxies for enzymatic reaction rates[22-24]. Hypothesis-free testing of ratios between all possible metabolite pairs in tissue extracts analyzes by GWAS and MWAS have provided an innovative approach for discovery of new biologically meaningful molecular associations[25]. Furthermore, metabolite ratios from tissue extracts have been used to construct large scale neural networks that improve statistical assessments and facilitate data interpretation[26]. Despite the promising applications of metabolite ratio analysis to enhance knowledge obtained from omics datasets, there has not been a reported computational approach that enables untargeted spatial imaging of all metabolite pairs in an MSI dataset.

To fill this perceived gap in MSI analytical tools, we developed a computational approach for untargeted imaging of ratios comprising all detected known and unknown metabolites in every pixel of an MSI experiment. While individual metabolite ion abundance levels in spatial metabolite profiling studies fail to inform on the activity of metabolic pathways, or on the identity of metabolic intermediates contributing to a metabolic pathway, pixel-by-pixel imaging of the ratio of an enzyme's substrate and derived product offers an opportunity to view the distribution of a functional activity for a given metabolic pathway across a tissue cryosection. In this report, we use exemplary MALDI MSI data obtained from cryosections of murine embryos, brains and a mitochondrial myopathy model of tissue derangements to demonstrate the application of ratio imaging as a tool to recognize both normal and pathology-associated regio-specific perturbations in metabolic pathways. We demonstrate that ratio imaging minimizes systematic variations that may be introduced into MSI data by sample handling and instrument drift, improves overall spatial image resolution, enables the anatomical mapping of metabotype heterogeneity, facilitates biomarker discovery, and can serve to discover new spatially resolved tissue regions of interest (ROIs) that are metabolically distinct but otherwise unrecognized. Further, using murine embryo and hippocampus MALDI MSI data acquired at single cell spatial resolution, we showcase the potential of single cell metabolite ratios to probe metabolic enzyme activities, as well as the potential for integration with other datasets obtained using additional multiomic data acquisition platforms. Importantly, the algorithm for ratio imaging described here should be applicable to spatial MS profiling of all sorts, including metabolites, peptides and proteins. This software package is being made available as a powerful add-on tool that can enhance the information obtained from conventional spatial metabolite profiling analyses.

Experimental

Sample preparation. Brain and adipose tissues from a mitochondrial myopathy model of cytochrome c oxidase assembly factor heme A:farnesyltransferase COX10 knockout (COX 10 KO) and wildtype (WT) mice and adipose were frozen in liquid nitrogen and stored at −80 °C until processing. Entire mouse decidua dissected from pregnant females at gestation day 8.5 were embedded in 2% carboxymethylcellulose, frozen in liquid nitrogen, stored at -80°C, and sectioned at 12 µm nominal thickness. Brain cryosections were cut at 10 *µm* and adipose at 20 µm thickness (n=4 or 3 per group), mounted on conductive slides coated with indium tin oxide (ITO; (Delta Technologies; cat # CB-90IN-S111) and stored at -80°C. On the day of MALDI MS data acquisition, ITO-slides with tissue sections were transferred to a vacuum chamber and dried for 30 min prior to deposition of desired matrices for imaging: N-(1-naphthyl) ethylenediamine dihydrochloride (NEDC; 10 mg/ml in 75% methanol) for murine brain and E8.5 embryos; 1,5-diaminonaphthalene (DAN, 2 mg/mL in 50% acetonitrile) for murine COX10 KO adipose tissues, and 9-aminoacridine (9AA, 5mg/ml in 85% Ethanol) for murine hippocampus. All matrices were delivered using an HTX TM-Sprayer™ (HTX Technologies LLC, NC) with optimized spraying parameters for each individual matrix. Matrix-coated tissue sections were dried in vacuum desiccator for 20 min before MALDI MSI data acquisition in negative ion detection mode.

MALDI MSI data acquisition and processing. MALDI MSI data were acquired at raster width of either 10 µm or 80 µm using a 7T scimaX-MRMS mass spectrometer (Bruker Daltonics, USA) equipped with a SmartBeam II laser and a MALDI source. Peak-picked MALDI-IMS data were imported into SCiLS Lab 2023a software (SCiLS, Bremen, Germany) for image visualization. Compound identifications were assigned based on both accurate mass (<2 ppm mass accuracy) and isotope pattern matches to free source metabolite and lipid databases, including the Human Metabolome Database (HMDB), KEGG and LIPIDMAPs. An in-house R-code developed for the programmable Scils Lab Application Interface (Scils lab API) was used for fast export of raw pixel-by-pixel metabolite and unknown mass spectral abundance data from regions of interest (ROIs) and whole tissue sections. Missing abundance values for metabolite/feature at a given pixel was imputed as 1/5 of its minimum detected abundance among all pixels for that m/z species. Pixel-by-pixel metabolite ratios for detected metabolites/features were calculated using minimum-annotated pixel data. Differential metabolite ratios among ROIs were visualized in R and exported as either an image or PDF file. Figure 1 depicts a schematic workflow using Scils Lab API for metabolite ratio imaging and associated multivariate analysis among ROIs. Notably, a series of Scils lab API R codes for ratio imaging visualization, data analysis, PCA and segmentation are available for download on GitHub. For MSI data acquired from other non-Bruker MS imaging instruments, R codes are also available to extract pixel data directly from imzml file, a common data format for MS imaging, using Cardinal 3.0 free-source software and the resulting pixel data can be applied for ratio imaging (Fig.1).

Results

1. Generation of an untargeted spectral feature list for export of pixel data to enable downstream metabolite ratio analysis. Using Scils lab API, we sought to establish new data processing and analysis features that can be utilized for metabolite ratio imaging. Toward this end, we developed an R code that engenders fast export of raw or normalized pixel-by-pixel feature abundance data for all sections and/or regions of interest (ROIs) in an EXCEL.csv file format. A targeted feature list from metabolic pathways of interest can also be imported into Scils lab as .mir files, generated using either a Python program or a Scils lab feature list with manual ID annotation of peak-picked spectral data. Multiple feature lists from different metabolic pathways of interest can be saved for exclusive ratio imaging of these designated pathways. Once pixel data are available, a Scils lab license is no longer required for metabolite ratio imaging and downstream statistical analysis, except for label and spot image generation within the Scils lab environment. Notably, EXCEL format pixel data directly extracted from imzml files of other vendor's proprietary MSI instrument software are also amenable to the ratio imaging strategy described herein.

Importantly, pixel-by-pixel metabolite imaging data can be co-registered with other omics imaging datasets obtained from a sequential serial cryosection, independent of the need for a Scils lab license. Given the lack of need for proprietary software to export pixel-by-pixel data, an individual feature list provides MALDI-MS instrument/application flexibility. Additionally, considering each pixel data as a replicate from a defined ROI, exported pixel data can also be used for multivariate spatial metabolomics data analysis using either vendor-specific or non-proprietary metabolomics data software platforms[27-39]. Figure S1 shows an exemplary conversion of ROI pixel data to formats compatible with import into MetaboAnlayst[27] and Agilent Mass Hunter Professional, allowing for multivariate statistical analysis and biomarker discovery. For the presented demo data, brain outer cortex regions were selected for comparison between mitochondrial cytochrome oxidase 10 (COXKO) and WT (n=4 for each genotype) mice. Notably, exported pixel data obtained in this manner can be readily used by available metabolomics software platforms to perform conventional multivariate analyses such as PCA, PLS-DA, HCA, ROC curve assessment, VIP scoring and pathway enrichment.

2. Annotating missing pixel abundance is required for MSI ratio imaging. Missing value annotation is conventionally employed for interpretation of omics data, including metabolomics[40-43]. Spatial metabolomics data acquired from MALDI and DESI MSI studies are subjected to missing value annotation when features are undetected in a given pixel. Importantly, given the differences in cell types and ionization efficiency/suppression across tissue regions, missing values are more common in spatial MSI data compared to acquired LC/MS from the same tissue, especially in the case of FT-ICR-MS which uses a peak-picking threshold to filter out the bulk of signal noise generated from Fourier data transformation. To prevent the potential inclusion of “zero” abundance as a missing value for imaging data analyses that include mean ROI metabolite abundance comparisons for analysis of ROC curves, PCA, HCA and other assessments of metabolite ratio images, we annotate missing values with 1/5 of the minimum value for metabolites/features quantified all pixels in which it is detected. Figure S2 A-B shows the indistinguishable images of exemplary metabolites before and after missing value annotation[27]. Therefore, pixel-wise missing value annotated data was used for all statistical analysis, image plots and metabolite ratio imaging described in the method described herein. To provide reciprocal and complementary images for easier ROI access and visualization, we consider images for both A/B and B/A ratios (*see* Fig S2 C-D).

3. Pixel-by-pixel ratio imaging reduces cryosection preparation artefacts and enables better data interpretation. Preparing cryosections from non-fixed and non-embedded tissues is a technically demanding procedure that is prone to sectioning artefacts[44]. Indeed, tissue freezing, cryo-cut temperature variation, section thickness irregularities and tissue storage can all affect imaging performance. Additionally, non-lipid small molecule metabolites are known to suffer from smearing and/or diffusion during cryosection processing, including over the course of matrix deposition for MALDI-MSI. Ratioing of metabolite/feature abundance pairs pixel-by-pixel, offers the important advantage of reducing section processing artefacts often seen on slides, especially slides containing multiple tissue cryosections. Such artefacts often arise from non-uniform matrix coating of cryosections and the fact that individual cryosections are thaw-melted onto slides and the sequence of layout and waiting times for each section for completion of the mounting process commonly results in varying degrees of metabolically-active metabolite degradation, even at the typical -20°C cryotome operating temperature.

Figure S2A and Figure 2 A-C compare images for lyso-phosphoethanolamines (lyso PE 18:1, 20:4, 22:4, 22:6) on brain sections from COX 10 KO and WT mice. Lysophospholipids contain a free hydroxyl moiety in either the sn-1 or sn-2 position of the glycerol backbone and are generated by phospholipase (PLA1 and PLA2, respectively) mediated hydrolysis of phospholipids. PLA1 hydrolyzes an ester bond at the sn-1 position producing a saturated or mono-unsaturated fatty acid and a 1-lyso-2-acyl-phospholipid, while PLA2 preferentially hydrolyzes unsaturated fatty acids at the sn2 position, producing poly-unsaturated fatty acids and 2-lyso-1-acyl-phospholipid. Notably, Lyso PEs with polyunsaturated acyl chains of 20:4, 22:4 and 22:6 shown in Figure 2 appear to predominantly originate from PLA1 action. As shown, images

of these individual LPEs are relatively diffuse and variable among replicates of same genotype (Fig 2 A-C). A relatively higher abundance of these species was imaged in cross-sections of the striatal ventral region of the brain, except for LPE 22:6 in COX 10 KO brain, which was more abundant at the outer cortex. Note that 20:4 and 22:4 acyl chain derived from ω6 fatty acid arachidonic acid (20:4) and adrenic acid (22:4), while 22:6 acyl chain originates from ω3 fatty acid, docosahexaenoic acid (DHA). Ratio images of LPE 20:4 and LPE 22:4 to LPE 22:6 would indicate the higher abundance of ω6 to ω3 containing PEs in the striatum ventral region compared to the outer cortex region of the brain (Fig 2 D-F), which is consistent with the distribution of abundance ratio arachidonic acid to docosahexaenoic acid (Fig 2G). Compared to the blur and diffused non-ratio images of individual lyso PEs, ratio images of ω6 and ω3 lyso PEs show an enhanced brain structure with markedly sharper image definition. Despite a variable lyso PE value imaged in COXKO and WT brains, the overall ratios of lyso PEs did not change between genotypes. Note that we purposely chose this set of non-ideal section quality and imaging data to demonstrate the clear benefit of ratio imaging to obviate potential cryosection and sample processing artefacts, resulting in improved image quality for data interpretation.

4. Targeted metabolite ratio imaging reports spatial enzyme and pathway activities. When substrate-product metabolite pairs for an enzyme are used for pixel-by-pixel ratio imaging, pixel-wise specific enzyme activity distribution can be implied. Several product-substrate metabolite ratios may serve as readouts for comparative enzyme activities such as: glutamine to glutamate for glutaminase (GLS), aspartate to asparagine for asparagine synthase (ASNS) , N-acetylasparate to aspartate for N-acetyltransferase 8 (NAT8) , inosine monophosphate (IMP) to adenosine monophosphate (AMP) to for AMP deaminase (AMPD), lactate to pyruvate for lactate dehydrogenase (LDH), N-acetyl-aspartyl-glutamate (NAAG) to N-acetyl-aspartate for NAAG synthetase (NAAGS), carnosine to histidine for carnosine synthase (CARNS), hexose phosphate to hexose for hexose kinase (HK), glutamate to oxyproline for 5-oxoprolinase (OPLAH), glutathione disulfide to glutathione for glutathione peroxidase (GPX) etc. Fatty acids are synthesized through metabolic pathways that include desaturation and elongation, sequentially producing a variety of long-chain saturated, monounsaturated, and polyunsaturated fatty acids (SFA, MUFA, and PUFA, respectively). Palmitic acid (FA 16:0) and stearic acid (FA 18:0) are the most common and abundant long chain saturated FAs in food and the human body. MUFAs synthesized from SFAs via stearoyl-CoA desaturases (SCDs), serve as key component of phospholipids, triglycerides, and cholesterol esters that serve to modulate cell membrane fluidity.

For lipid related metabolites, ratios between different number of fatty acid (C16, C18, C20) double bonds would imply fatty acid desaturase (SCD) activities. Similarly, the fatty acid synthase (FAS) and PLA activities can be reflected by assessment of the ratios of fatty acids with 2 carbon differences and phospholipids vs. corresponding lyso-phospholipids. Obviously, pixel-by-pixel metabolite ratios only becomes possible for metabolite pairs that are detected and imaged within the same pixel on a given tissue cryosection. MALDI MSI using NEDC matrix and negative ion mode detection can detect all of the above-mentioned substrate-metabolite pairs. In fresh cryosection preparations using 9-Aminoacridine (9AA) as a matrix, purine and pyrimidine nucleotide mono-, di- and triphosphates can be imaged to obtain pixel-by-pixel ratios of nucleotide with different phosphate levels for pixel-by-pixel assessment of the relative phosphorylation status in a tissue.

Figure 3 depicts the benefit of imaging metabolically relevant metabolite ratio pairs as a means to assess potential regional gradients in enzymatic and metabolic pathways, as exemplified in E8.5 embryos at 10 µm (cell-based) spatial resolution. Consistent with a role for the visceral yolk sac in providing nutrients, including glucose for embryo development, enhanced glycolytic activity was seen in the amnion and visceral yolk sac (Fig 3 A-B). Furthermore, higher abundances of the desaturase product FA 18:1 relative to FA 18:0 and of PE 38:4 relative to PE 18:0 (reflecting PLA2 activity) dominantly locate in the allantois and head mesenchyme with greatest abundance in the hindbrain neuroepithelium (Fig 3 C). In contrast, the embryonic ratios of saturated FA 16:0 relative to its elongation product FA 18:0, and DHA (ω3) relative to AA (ω6) fatty acids, show the opposite spatial distribution patterns (Fig 3 D-E). Of note, similar ω3 to

ω6 fatty acyl chain composition was also observed for lyso PEs (Fig 3 F-G). Interestingly, PLA1 and PLA2 appear to have quite different compartmented activities among yolk sac, amnion, and head mesenchyme (Fig 3 G-H). These data offer promising and useful information for study of compartmented metabolism during embryo development at the single cell level, demonstrating the power of metabolite ratio imaging for insights into the spatial assessment of metabolic activities.

As an additional example, we present mouse hippocampus MSI findings which confirm that ratio imaging can resolve cell-type specific metabolic activity at cellular (10 μm) spatial resolution. Notably, neurons are known to have higher energy level and prefer mitochondrial oxidative phosphorylation as their dominant energy source. In accord with this expectation, higher ATP/ADP, ADP/AMP, ADP/AMP, IDP/IMP ratios (Fig 3 J-L) are all observed in neurons of mouse hippocampus, while indicators of oxidative stress (Fig 5 I) and fatty acid synthesis (Fig. 3 P) do not change in neurons compared to other cell types. Elevated SCD and AMPD activities were also predominantly observed in neurons (Fig 3 M-N) compared to other cell types, consistent with SCD being a novel regulator of neuronal cell proliferation and differentiation and reported immunocytochemical results[47]. Although a higher ratio of ω3 to ω6 fatty acids predicts relatively better hippocampus-dependent spatial memory and cognitive status in older adults[48], ratio imaging surprisingly shows that these neurons display a relatively lower level of DHA (ω3) to AA (ω6) fatty acids vs. other cell types in mouse hippocampus. Thus, ratio imaging findings can raise questions that challenge concepts demand further investigation.

Adipose tissues store body fat as neutral triglyceride and represent the chief energy reservoir within mammals. We have reported that COX 10 KO mouse are typified by decreased white adipose stores, accelerated lipolysis with increased free fatty acid deposition and low leptin levels with decreased food intake[49]. We have since applied lipid and fatty acid ratio imaging to evaluate potential metabolic and enzyme activities that may be responsible for lipid and fatty acid metabolic features in adipose tissue of COX 10 KO compared to WT mice (Fig 4). As expected, distinct fatty acid and lipid profiles pointing to altered ω3 (DHA) to ω6 (AA) fatty acid composition (Fig 4 A), fatty acid and lipid desaturation (Fig 4 B-G), fatty acid synthesis (Fig.4 H-J) and phospholipid hydrolysis (Fig 4 K-L) are observed in COX 10 KO vs. WT adipose tissues. It has been shown that lower adipose ω3 to ω6 ratio is associated with tissue inflammation[50], obesity[51], altered gut microbiota[52,53] among other health problems[54,55]. These ratio imaging findings led us to speculate that the diminished ω3 to ω6 ratio arises in COX 10 KO mice from an altered gut microbiota population, supported by unpublished preliminary findings. This emergent hypothesis from ratio imaging analysis raises the clinically important possibility that hypothesis that supplementation of human COX 10 mutant patients with ω3 fatty acids (such as DHA) may provide an opportunity to effectively modify microbiota populations in a manner that restores towards a more normalized adipose tissue composition and food intake.

As shown, ratio imaging uncovered an altered adipose fat profile with diminished FA desaturation (Fig 4 B-G), elevated elongation (Fig 4 H-J) and enhanced phospholipase activity (Fig 4 L-M). Ratios of an array of phospholipids (PA, PE and PC) containing longer fatty acyl chain length vs. shorter fatty acyl chains were also increased in COX 10 KO adipose (data not shown). These results suggest that fatty acid synthesis (elongation from FA 16:0) may be upregulated, outcompeting desaturation by SCD to FA 18:1 in COX 10 KO mice. Consistently, several key enzymes in fatty acid synthesis pathway including FAS were upregulated in COX 10 KO adipose (not shown). Since fatty acid synthases (FASs) are predominantly regulated at the transcriptional level by nutrients and hormones, their upregulation could result from relatively attenuated FA and other nutrient uptake from food. Moreover, as loss of SCD activity induced leptin resistance in neuronal cells[56], downregulation of SCD activity, as indicated by FA ratios, may explain disrupted leptin signaling as a basis for altered food intake in COX 10 KO mice[49].

Taken together, these results demonstrate the utility of ratio imaging as a valuable new approach for analysis of MSI data to probe for potential regiospecific changes in cellular metabolic activities.

5. Metabolite ratio uncovers genotype-specific and spatially resolved tissue regions. Conventional MSI depicts relative spatial abundance of metabolite features in tissue regions. For defined structures in tissues such as brain, kidney and prostate, metabolite images can potentially recognize discrete tissue structures, under the condition that ionization efficiency and/or absolute abundance differences do indeed exist among these structurally defined loci. In contrast, pixel-by-pixel metabolite ratio imaging almost invariably resolves distinct tissue structures but also uncovers fine structure and anatomically unrecognized regions that are not revealed by individual metabolite imaging alone.

Using COX10 KO and WT mouse coronal brain sections as an example, we observed that individual glutamate, aspartate and glutamine distribution images failed to show a clearcut structural distribution, possibly due to diffusion of these hydrophilic metabolites (Fig 5 A-C). However, ratio imaging showed a relative much greater aspartate to glutamate abundance ratio that resides in an unusual "moon arc" region across the amygdala and hypothalamus region of the coronal brain. Similar but different arc-like structures are encompassed within the ventral thalamus and hypothalamus wherein a higher abundance of glutamate to glutamine ratio is observed (Fig. 5 D-E). while relative glutamine to aspartate abundance appears to be enriched in striatum region (Fig. 5 F). Thus, ratio images not only improve image quality for regional/cell-selective assessment of metabolite distributions, but also offers an opportunity to discover new differentially metabolic regions with potential biological relevance. Note that the enrichment of aspartate to glutamate and glutamine to glutamate near thalamus, nucleus accumbens (NAc) and hypothalamus region of brain (and visualization of their reciprocal ratio images) were found to be robust and consistently reproduced in MALDI MSI experiments using an independent cohort of COX 10 KO and WT mouse brains (Fig. G-H). Enrichment of glutamate to aspartate in the cortex region was further confirmed in horizontal and sagittal brain sections from random mouse brains (Fig 5 I-J).

Considering the above findings, it is notable that aberrations in glutamate, glutamine and aspartate homeostasis are all implicated in neurological diseases[57,58]. Aspartate serves as amino donor for glial glutamate formation[59] and the hippocampal aspartate to glutamate ratio has been related to changes in brain glucose[60]. Glutamine is synthesized from glutamate and ammonia by the catalytic action of glutamine synthetase (GS) in glial cells of the brain, while it is also taken into neurons and generates glutamate and ammonia by the catalytic actions of glutaminase. The glutamate-glutamine cycle is closely linked to cellular energy metabolism[58] and ratios between neurotransmitters (GABA, glutamine and glutamate) have been used in MRS studies to probe neurological disease mechanism and progression[61,62]. Specifically, ratios among glutamine, glutamate and aspartate have been implicated in memory function[63], schizophrenia, depression, alcoholism and motivated performance via NAc[64]. Given the biological significance of these ratios, spatial ratio imaging can reveal hitherto unrecognized ROI and relative ratio abundance differences between disease and normal physiological states. In COX 10 KO and WT brains, differential aspartate to glutamate and glutamine to glutamate ratios point to an interesting linkage between muscle health and brain neurotransmitter signaling: mitochondrial myopathy alters glutamine, glutamate an aspartate signaling near the NAC regions of the brain. This unusual finding is in accord with and supportive of our recent discovery of a coordinated multiorgan metabolic response that extends to brain and is anticipated to play a role in human mitochondrial myopathy disease states[49].

6. Spatial correlation of ratio and non-ratio pixel-by-pixel data as an additional discovery tool. Metabolite ratio imaging enables deeper mining of spatial imaging data relative to consideration of individual metabolites alone. However, combining pixel-by-pixel ratio and non-ratio pixel data offers an additional tool in the armamentarium of strategies for spatial metabolism discovery. This application can reveal unrecognized but significantly correlated pathway metabolites and metabolite ratios that enable the recognition of unknown metabolites that have relevance to specific pathways of interest. Despite that MALDI MSI is a soft ionization technique, it generates various adduct ion clusters and possible fragment ions from common neutral losses.

Unknown non-ratio metabolite feature data for every pixel in a given ROI can be combined with known metabolic pathway metabolite ratios, pixel-by-pixel, as a means to discover correlations between unknowns with metabolite ratios that inform on a specific enzyme activity or metabolic pathway. Using COX 10 KO and WT mouse adipose tissues as an example, the unknown [M-H] 375.23059 was found to negatively correlate with the ratios PA 36:4 to LPA 16:0 and PA 36:1 to PA 18:1, indicating the abundance of this unknown metabolite may be positively associated with phospholipase PLA (PLA2 and/or PLA1) activity (Table1**).** Given that PLA1 and PLA2 each generate different lyso-phospholipids, with PLA1 dominantly yielding unsaturated lyso-phospholipid products and PLA2 yielding saturated lyso-phospholipids. An observed negative correlation of the unknown with LPA 18:1 to LPA 18:0 ratios suggests the possibility that it may originate as a product of PLA2. Indeed, direct correlation of this known with lipid metabolites suggest that it could be a reduction product of CPA 16:0 after loss of one oxygen atom, matching the formula $C_{19}H_{37}O_5P$ with a mass accuracy of 0.013 ppm. While it remains to be established that this unknown is indeed a *bona fide* reduction product of CPA 16:0, this example serves as an illustration of how pixel-by-pixel correlations of unknown metabolite masses can be combined with metabolite ratios as a tool for potential discovery of pathway-relevant metabolites.

Another example of correlation-based discoveries comes from consideration of COX 10 KO and WT mouse brain sections, where calculating the Spearman correlation of combined pixel data from both metabolite alone and metabolite ratios revealed an unexpected positive association of $FeCl_2$ with the glutamate to glutamine ratio, along with other related metabolite ratios that include aspartate, NAA, glucose and glutathione (Table 2, Figure S3). Conversely, glutamine to glutamate ratios show a significant negative correlation with $FeCl_2$ and the above-mentioned metabolites (Table S1), suggesting that these correlations are not random and are not an artefact of missing value annotation with minimum values. Notably, free iron is recognized as a key mediator of glutamate excitotoxicity in spinal cord motor neurons[65]. Significant associations between peripheral markers of iron metabolism and glutamate with glutamine in relation to total creatine (Glx:tCr) concentration has been reported in female human brains[66]. Glutamate facilitates divalent metal transporter 1 (DMT1) flux and subsequent increases in brain free iron content[67]. A positive relation between iron and glutamate in the brain and other organs has also been reported[65,66,68,69,57,58].

Note that this correlation with $FeCl_2$ was observed in all brain sections regardless of genotypes of their COX 10 KO and WT genotypes. Ferrous iron, measured as its chloride adduct when detected with NEDC matrix, likely arises from both free labile iron and protein-bound iron. Decreased $FeCl_2$ levels in combination with decreased glutamate level in the cortex region of COX 10 KO vs. WT mouse brain is an unexpected but intriguing finding. While aging is associated with increased brain iron through cortex-derived hepcidin expression[70], calorie restriction down-regulates expression of the iron regulatory hormone hepcidin[71]. In accord with decreased Fe^{2+} and glutamate to glutamine ratio, COX 10 KO mice showed decreased food intake and adapted a metabolic state resembling caloric restriction[49]. Collectively, pan-correlation of targeted metabolite ratios of interest with and non-ratio data serve as an add-on tool for imaging data interpretation and novel hypothesis generation.

7. Metabolite ratios for PCA tissue segmentation in complex tissue sections. Spatial segmentation is a popular application in MSI to cluster regions with similar metabolite abundance profiles. Unsupervised MSI segmentation methods such as principal component analysis (PCA), K-means, bisecting K-means and hierarchical clustering (HCA) are all often used to delineate the underlying tissue structure from high-dimensional MSI data without prior knowledge of sample anatomical information. Most segmentation approaches rely upon unsupervised clustering algorithms that can readily result in the generation of biologically unrealistic tissue structures. Various algorithms for integrating partial or prior structural information with unsupervised clustering have been reported to improve the segmentation results[72-78].

Up to now, tissue segmentation has not been reported which utilizes pixel-by-pixel metabolite ratio data for imaging differential metabolic zones. We hypothesized that metabolite/feature ratios may generate more meaningful biologically relevant ROIs due in part to a systematic experimental noise reduction. Mouse brain sections serve as a good example for the utility of this approach. As expected, consideration of a group of 10 different glutamate/glutamine related metabolites for PCA analysis (Table S2), with ratios involving the top 5 components in mouse brain generating an interesting arch shape region that encompasses the hypothalamus, striatum and NAc, while non-ratio metabolite alone data did not (Fig 6A). Note that this metabolite ratio PCA result was used to provide an RGB image that captures the structure of the dataset by mapping the first the five principal components. Apparently, this segmentation result captures and maintains the enriched arc-like regions shown previous in neurotransmitter ratio images (Fig 5 D-E and G). Since glutamate plays key roles linking carbohydrate and amino acid metabolism via the tricarboxylic acid (TCA) cycle, as well as in nitrogen trafficking and ammonia homeostasis in brain, it is likely that this region exhibits unique glutamate-related metabolism that warrants further investigation. Likewise, a more defined outline of striatum and cerebellum in the coronal brain structure was obtained in PCA segmentation using top 5 component metabolite ratios as well as 5 phosphoethanolamines (PEs, Table S3), but not observed with these 5 PEs alone (Fig.6 B).

As metabolite ratio data can segment tissue into ROIs that are unrecognized by conventional metabolite alone data, we considered the possibility that differential metabolite ratios can serve as independent marker (or combined with individual metabolites) as a means to distinguish genotypes. Brain contains various small molecules that act as neurotransmitters and coordinate neural communication. In COX 10 KO and WT mouse brains, ratios among three neurotransmitter-related non-glutamate metabolites (glutamine, aspartate and homocarnosine) show clear differences in COX 10 KO compared to WT, at the cerebral cortex for glutamine to aspartate ratio (Fig 7A) and within the ventral striatum for homocarnosine to glutamine and homocarnosine to aspartate ratios (Fig 7 B-C).

The interrelationship of glutamine, aspartate and homocarnosine is shown in Fig 7D. Homocarnosine is a naturally occurring imidazole-containing dipeptide uniquely present in the brain, likely in a subclass of GABAergic neurons[79]. It is synthetized from γ-aminobutyric acid (GABA) and histidine via homocarnosine synthase (CARNS1) and can be hydrolyzed to histidine and GABA by carnosine dipeptidase 1 (CNDP1) which is exclusively expressed in brain (Fig 7D). Homocarnosine is recognized to play a role in mediating neuronal activity during satiation and starvation[80]. It is decreased in the brain during cold adaptation[81] and increased during alcohol intoxication[82]. Additionally, it is well known that aspartate and glutamate can be exchanged across the inner mitochondrial membrane by mitochondrial carrier protein SLC25A12 (aka. Aralar1), mainly distributed in brain and skeletal muscle for the transport of aspartate from mitochondria to cytosol, and in the transfer of cytosolic reducing equivalents into mitochondria as a member of the malate-aspartate shuttle[84]. Given the inter-relationship of these three metabolites and their important role in maintain brain neurotransmitter pools, their ratios could report on neurotransmitter homeostasis. Indeed, it has been shown that brain function can be estimated from the ratio of glutamine to homocarnosine levels in cerebrospinal fluid[85]. An early report showed that homocarnosine is elevated in monkey brain in the setting of a protein-deficient diet, whereas aspartate and glutamate levels are unchanged[86]. Similarly, in COX 10 KO and WT brains we observe no differences in individual aspartate or glutamate levels (Fig 5 A-B) while striatal homocarnosine (Fig 7E) and glutamine (Fig 5C) levels were elevated. As COX 10 KO mouse displayed an altered food intake, muscle mass and elevated starvation response[49], an elevated homocarnosine to glutamine and glutamine to glutamate ratio (Fig 5F) could indicate an increased synthesis of homocarnosine via the route of glutamine-glutamate-GABA axis. These results indicate that ratios among the three metabolites could serve as alternative markers with the ability to clearly distinguish these murine genotypes.

In attempt to provide additional spatial detail, we performed PCA segmentation on COX 10 KO and WT brains using non-ratio and ratio pixel data of homocarnosine, glutamine and aspartate with the goal to

learn whether differential ROIs exist for these genotypes. In this PCA segmentation with top 3 principal components, the overview RGB image maps the first three principal components to the red, green and blue channels respectively. Comparing PCA overview images from ratio (Fig 7F) to non-ratio (Fig 7G), PCA results from ratio show cyan blue located in larger area of striatum, thalamus, regions in KO relative to WT brains, while non-ratio PCA result did not. These results indicate distinguishable abundance in the cyan region of the KO and WT brain regarding the interconversion and homeostasis of three neurotransmitter-relevant metabolites. Therefore, metabolite ratio could serve as better candidates for ROI-based disease metabotyping.

8. UMAP using metabolite ratios enables spatial metabotype mapping and recognizes novel ROIs. Unlike PCA analysis which builds on a linear dimension reduction algorithm, uniform manifold approximation and projection for dimension reduction (UMAP) is a relatively newer non-linear dimension reduction algorithm that is often used to visualize complex dataset while preserving local structure. UMAP projects dimensionally reduced data into 2D or 3D scatterplots. Samples that are close to each other in the scatterplot have similar fingerprints, while samples that are further away have progressively different profiles. It is often used in combination with other clustering algorithms such as HCA and K-mean clustering to identify subgroups in the projected space. UMAP has been widely used for omics data interpretation to find internal structure in mixed data sets, as well as for disease subtyping, single cell bioogy[87-89] and in various molecular imaging applications.

Since metabolite ratio segmentation using PCA is less prone to section preparation artefacts in MALDI MS and enables genotype-specific tissue segmentation (Fig 7F), we sought to assess whether metabolite ratio UMAPing and clustering can generate novel ROIs that enable new spatial metabotype mapping in advance of which may be obtained from consideration of only individual metabolites. UMAP analysis of ratios for a group of 5 lysophosphatidylethanolamines (LPEs) in COX 10 KO and WT murine brain sections, followed by K-mean clustering, showed a much more defined and biologically relevant ROIs vs. those considering non-ratioed LPEs (Fig 8) that resemble PCA segmentation results (Fig 6B). Note that this analysis used 9 neighbors with 2 Euclidean components as metric measurement of similarities for this UMAP analysis. Figures S4-5 show the nine segmented ROIs from non-ratio and ratio UMAP and K-mean clustering analyses, along with scatterplots of the first 2 UMAP components (V1 vs V2), projecting the distribution and similarity of each of 9 segmented ROIs. While the non-ratio segmented ROIs did not provide comparable and confident ROIs among replicates (Fig S4), the ratio-segmented data indicate a distinct LPE profile between outer cortex (ROI 3), cortex (ROI 8), ventral thalamus (ROI 5) and striatal regions (ROI 2) (Fig S5). These ROIs generated by UMAP metabolite ratios not only enable visualization and a reproducible comparison of lipid metabolite and/or ratio abundance among these irregular and difficult-to-draw (i.e., with imprecise anatomical definition), but also provides unique ROIs for pixel-by-pixel metabolite correlation with other multivariate analyses mention previously (Table 1, Fig S1).

Difference in metabolite image abundance among ROIs can be difficult to visualize if the image color scale is set too wide. ROI images are better visualized by applying a relative image abundance scale set to a discrete ROI, rather than the entire tissue section. UMAP segmentation using ratios provides novel ROIs for such a purpose. For example, murine brain imaging results show decreased aspartate to NAA ratio visualizable in almost all 8 ROIs investigated with COX 10 KO, suggesting an overall diminished expression or activity of N-acetyltransferase (NAT8L), the neuronal enzyme that produces NAA from acetyl-CoA and aspartate (Fig S6 A-H). Moreover, N-acetyl-aspartyl-glutamate (NAAG), the most abundant dipeptide in the brain, can be synthesized from NAA and glutamate by NAAG synthase. NAAG to NAA and aspartate ratios are shown to be greater in ROI 7 of COX 10 KO compared to WT (Fig S6 I-J), suggesting an elevated NAAG synthase activity in this defined region. Of note, NAT8L mRNA oxidation is linked to neurodegeneration in multiple sclerosis[94] and overexpression-induced vulnerability to depressive behavior in mice[95]. NAAG functions as a retrograde neurotransmitter and is released in

response to glutamate, providing the postsynaptic neuron with a feedback mechanism to inhibit excessive glutamate signaling[96]. Therefore, elevated in NAT8L activity, indicated by an increased NAA to aspartate ratio, is consistent with observations that COX 10 KO mice are less mobile and relatively inactive compared to WT. Reviewing the non-ratio images of these NAT8L related metabolites, NAAG is mainly enriched near ROI 7 visualized in whole section images (Fig S7 A), consistent with higher abundance of NAAG, NAA and glutamine imaged exclusively in COX KO ROI 7 (Fig S7 B-D). These changes contrast with decreased aspartate and no change in glutamate levels imaged in ROI 7 of COX 10 KO mouse brains (Fig S7 E-F). Therefore, we infer that the COX 10 KO brain exhibits increased NAA and NAAG syntheses as feedback to inhibit excessive glutamate signaling. In contrast, glutamate within the NAc region show no change compared to WT, potentially due to as excess glutamate being used for the synthesis of glutamine and NAAG which are elevated in KO in ROI 7 (Fig S7 C-D). Consideration of these UMAP findings exemplifies the applicability of this strategy for MSI data interpretation.

UMAP derived ROIs can be applied to survey metabolite abundances, pixel-by-pixel, for correlation analysis in RO1s from a large combined dataset that includes metabolite ratio and non-ratio pixel data, as shown previously in Table 1-2 for whole tissue sections. When correlation is narrowed down to a specific ROI and genotype, regional correlation results can be very different from global correlations. Fig S8 shows a pixel-by-pixel correlation of the ratio of glutamine to glutamate, along with a compendium of all detected metabolites and ratios contained in a UMAP-generated ROI 7, comparing WT to COX 10 KO brain. For an improved correlation plot visualization, only significant correlations with a spearman correlation coefficient of greater than 0.4 are presented in Fig S8. Glutamate to glutamine ratio positively correlated, while negative correlations were observed for glutamate/NAAG, and NAAG/NAA in both WT and KO ROI 7(Table S5) these findings are consistent with knowledge that NAAG synthesis inhibits excess glutamate signaling.

Given that LPE ratios can be used as a tool for brain segmentation and overcome variations in section quality, we asked if UMAP with the same 5 LPE ratios can similarly be applied for other types of brain section ROI segmentation. As predicted, UMAP generated ROIs consistent with brain anatomy in two separate experiments depicted by horizonal and sagittal brain sections (Fig S9).

Collectively, UMAP analyses using metabolite ratio imaging provides a novel and robust tool to spatially-map tissue microenvironments, revealing matched localized differences among test groups.

Discussion

Analyses that utilize metabolite ratios are not a new concept in omics investigations particularly for applications that involve medical MRI spectroscopy-generated imaging data. Notwithstanding, an unbiased strategy and application of pixel-by-pixel imaging of targeted/untargeted metabolite ratios in MSI studies has been lacking for the interpretation of spatial imaging metabolomics data. We demonstrate that ratio imaging adds a powerful new tool to mitigate sample preparation artefacts, for spatial metabotyping tissue microenvironments, and revealing spatially distinct functional variations in enzymatic and metabolic pathway activities.

Metabolite ratio imaging can serve to uncover previously unrecognized biology, as exemplified here for the pixel-by-pixel distribution and metabolic interplay among neurotransmitter related metabolites in the brain. Glutamate, glutamine, aspartate, histidine, homocarnosine and GABA are all well-recognized brain metabolites that contribute importantly to fundamental brain activities, including synaptic transmission and energy production. Their ratios are tightly regulated for maintaining proper brain function and can vary across different regions of the brain and under different physiological conditions. Disturbance of

these ratios can have detrimental effects on neurotransmission and overall brain health. Imaging of ratios among these and all other metabolites engender a novel mapping tool that may point to localized segmentation of metabolic activities that are not recognized by individual metabolite imaging alone. Considering ratios are proxies of enzyme reaction rates between substrate and product, ratio-derived ROIs along with their ratio and non-ratio abundances offer a novel strategy for the study of disease pathophysiology, biomarker discovery and with the potential to reveal new therapeutic targets (Figs 5-7).

As we describe, untargeted pixel-by pixel ratios can be derived from all detected mass spectral features, irrespective of whether the features have assigned or unassigned structural identities. Combined with non-ratio feature data, information-rich metabolite ratio datasets offer great potential for association with other imaging or spatial omics data. Notably, generation of metabolite ratio datasets can be performed using the R-code algorithm that we describe here, applied to individual metabolite features pixel-by-pixel that have been incorporated into an excel csv format file with spot ID and pixel axis positional information. Furthermore, R codes for generating pixel data directly from imzml file provides a convenient way to perform spatial ratio analysis for all types of MSI experiments. For pixel data with a 10 µm raster width or less, single cell spatial imaging and omics data can ideally be associated with untargeted metabolite/feature ratio data to achieve single cell multiomics metadata integration. For this purpose, a P-gain can then be applied to filter out significantly correlated associations, as previously described for some well-established GWAS and MWAS association studies[22-25]. A potential challenge for single cell metabolomics spatial data interpretation lies in possible concerns regarding metabolite data co-registration with anatomical and/or other single cell omics datasets. Notably, when datasets are obtained from serial sections, a mere 10 µm shift could result in cell layer disparities.

Combined ratio and non-ratio pixel data offers a powerful new tool to survey significant but unappreciated global correlations between ratios of metabolites (both structurally defined and undefined) in distinct ROIs that are revealed by metabolite ratio tissue segmentation. Among other unexpected findings, we demonstrate that an elevated glutamine to glutamate ratio is observed in COX 10 KO compared to WT within the NAc region of mouse brain and that this ratio positively correlates with ferrous iron levels and Nat8L enzymatic activity (i.e. inferred from NAA to aspartate ratios, Table 2, Fig. S3 and Fig S7). It is important to point out that these associations were previously unrecognized but are consistent with a whole-body feed-forward action of mitochondrial myopathy on levels of brain leptin, corticosteroids and neurotransmitter signaling[49]

Applying targeted and untargeted metabolite ratios for PCA and UMAP tissue segmentation algorithms generates novel and artefact-free ROIs linking proxy metabolic activity. One limitation for MSI ratio data interpretation is that the coverage of known metabolite structures and pathways is considerably less (typically 2-3 hundred structurally identified species) than those surveyed by LC/MS analyses. It is important to note that combined ratio and non-ratio data can also be used for segmentation. However, segmentation result using combined ratio and non-ratio data may be confounded by artefact-prone non-ratio metabolite data and thus not as clean as those using ratio alone (data not shown). We speculate that combining metabolite ratios from different metabolic pathways may segment tissue with ROIs more representative of real metabotype.

In summary, targeted and untargeted metabolite ratio imaging is anticipated to provide a powerful add-on tool for the MSI field, revealing otherwise hidden information in acquired datasets. These ratios may serve as potential new biomarkers that distinguish anatomically distinct metabolic tissue regions that can uncover otherwise unrecognized differences in physiological cell functions, or which result from differing cellular responses to drug treatments and disease states. The strategy for ratio imaging can be further extended to imaging pixel-by-pixel fractional abundance of isotopologues for targeted and untargeted

MALDI MS stable isotope tracing. When coupled with the FTICR high resolution mass spectrometer, simultaneous imaging of isotopologue incorporation is possible for tracing molecules containing mixed stable isotope elements (e.g. ^{13}C, ^{15}N, ^{2}H, ^{18}O, ^{34}S).

Acknowledgements

We are thankful for Drs. Tal Nuriel, Eileen Ruth Torres, Li Gan for sharing mouse brain images used in this paper. NIH support by 1S10OD023652 (SG) for WCM's Ultra-high Resolution MALDI-FT-ICR Imaging Core Facility. NIH 5 R01 AR076029-03A1 (QC and MD), R21 NS118233-01A1 (QC and MD), R21 ES032347(QC).

Figure legends

Figure 1. Schematic workflow of metabolite ratio imaging using pixel data from Bruker Scils Lab API or imzml file from any MSI data source. For Scils lab MSI data, the execution of R codes starts with connecting a local Scils lab session project in R studio. Installation of Scils lab is required for this connection. After pixel data for a feature list is generated and exported as an EXCEL csv file, Scils lab installation is not required for downstream ratio imaging and data analysis, except for the potential writing of a spot image with labels back to Scils lab. For other types of MSI data, R code execution extracts pixel data from imzml file for subsequent ratio imaging and analysis.

Figure 2. Pixel-by-pixel ratio image visualization reduces cryosection preparation artefacts and enables spatial metabolic discovery in COX 10 KO mouse brain (left 4 sections) compared to WT (right four sections). Panel A-C: blurry and diffused images of lyso PEs with ω3 (A-B) and ω6 (C) polyunsaturated fatty acyl chains; Panel D-F: sharper ratio images of ω3 fatty acid containing lyso PE 20:4 and lyso PE 22:4 to ω6 fatty acid containing lyso PE 22:6; Panel G: ratio image of ω6 arachidonic acid (FA 20:4) to ω3 docosahexaenoic acid (FA 22:6) is consistent with the identified abundance ratio distributions for LPE 20:4 and LPE 22:4 to LPE 22:6.

Figure 3. Metabolically relevant metabolite ratio pairs that probe enzymatic and metabolic pathway activity in E8.5 mouse embryo cryosections and mouse hippocampus at 10 μm spatial resolution. Panel A: annotated drawing of E 8.5 embryo tissue, derived from the section adjacent to imaged section. Panel B-H: Ratio of substrate/ product pairs of glycolysis, fatty acid and lipid metabolism that imply compartmented activities for hexokinase (B), fatty acid desaturation (C), fatty acid chain elongation (D), fatty acid composition (E-F) and phospholipase activity (G-H) in E 8.5 embryos. Panel I-Q: Ratio images showing relative oxidative stress (I), adenine nucleotide energy levels (J-L), purine nucleotide cycle activity (M-N), fatty acid desaturation(O) and synthesis (P), ω3:ω6 FA ratio (Q), and composition in neurons (pink arrow), compared to other cells in mouse hippocampus.

Figure 4. Altered fatty acid and lipid metabolism probed by ratio imaging in adipose tissue from COX 10 KO vs.WT mice. COX 10 KO, left 4 sections; WT, right 3 sections. Imaging data was acquired at 80 μm spatial resolution. Panel A: Decreased abundance ratio of FA 22:6 (DHA, ω3 fatty acid) to FA 20:4 (AA, ω6 fatty acid) in COX 10 KO adipose tissue. Panel B-C: Decreased fatty acid FA 16:0 and FA 18:0 desaturation in COX 10 KO adipose. Panel D-E: Decreased desaturated fatty acid abundance ratios for lysophospolipids and phospholipids in COX 10 KO adipose tissue. Panel H-J: Elevated fatty acid synthesis inferred by free fatty acid and phospholipids ratios, considering FA 18:0 to FA 16:0 (H-I) and FA 20:1 to 18:1 (L) in COX 10 KO adipose. Panel K-L: Elevated PLA2 (K) and PLA1(L) activities implied by the elevated ratio of Lyso PA to PA in COX 10 KO adipose.

Figure 5. Ratio imaging uncovers novel mouse brain regions with genotype-specific and spatially resolved ratios of aspartate, glutamate and glutamine. Panel A-C: images of glutamine, glutamate and aspartate in coronal sections of COX 10 KO (left 4 sections) and WT (right 4 sections) mouse brains. Panel D-F: Differential abundance ratios of aspartate, glutamate and glutamine observed in defined regions of the COX 10 KO and WT brains. Panel G-H: Reciprocal and differential aspartate to glutamate ratio and Arc-like NAC containing region was repeated in a separate group of COX 10 KO (left 4 sections) and WT (right four sections) mouse brains. Panel I-J: Enrichment in the glutamate to aspartate ratio in the cortex region of mouse brain, as revealed in horizonal and sagittal sections.

Figure 6. PCA segmentation of mouse brains comparing ratio and non-ratio metabolite pixel data. Panel A: PCA considering the top 5 components from ratios of 10-glutamate related metabolites that reveal an

unanticipated arch-like regional distribution within the hypothalamus, striatum and NAc, that is not detected by consideration of only non-ratio metabolite data. Panel B: PCA considering the top 5 components 5-lyso PE metabolites showing fine brain structure that is not fully represented by only non-ratio metabolite segmentation.

Figure 7. Metabolite ratios for segmentation and biomarker discovery in segmented ROIs. KO: right 4 sections; WT: left 4 sections. **Panel A-C:** Ratio images of homocarnosine, glutamine and aspartate in. **Panel D:** Enzymatic regulation and interconversions among brain glutamine, aspartate and homocarnosine. **Panel E**: Image of homocarnosine. **Panel F**: PCA with top 5 components and using ratios of homocarnosine, glutamine and aspartate shows differential ROI abundance shown in cyan blue in larger area of striatum, thalamus hypothalamus regions in KO compared to WT. **Panel G:** PCA with top 5 components and using homocarnosine, glutamine and aspartate pixel data show indistinguishable ROIs between genotypes.

Figure 8. UMAP analysis using 5 LPEs ratio followed by K-mean clustering on COX KO and WT brain sections shows a much cleaner and biologically relevant ROIs compared to those of LPE non-ratio. **Panel A:** UMAP clustering using ratios of 5 LPEs. **Panel B:** UMAP clustering using 5 LPE pixel data. The list of 5 LPEs is shown in Table S3. Nine neighbors, 2 components with Euclidean distance as metric measurement of similarities were used in this UMAP analysis.

Supplemental figures

Figure S1 Application of pixel-by-pixel exemplary MALDI MS imaging data to metabolomics multivariate analysis using free or commercially available software package. Panel A: ROIs of COX 10 KO and WT brain outer cortex; **Panel B:** PLS-DA score plot showing classification of COX 10 KO and WT cortex pixels using Metaboanalyst 5.0 (https://www.metaboanalyst.ca/MetaboAnalyst/ModuleView.xhtml). **Panel C:** Variable importance in projection (VIP) scores of metabolites from PLS-DA shown in panel B. The colored boxes on the right indicate the relative concentrations of the corresponding metabolite in COX 10 KO and WT. **Panel D:** Matched pathways showing p values from the pathway enrichment analysis and pathway impact values from the pathway topology analysis. Differential metabolites imaged in cortex of COX 10 KO vs WT brain and metabolite quarries from KEGG mouse metabolic pathway were used in this analysis. **Panel E:** Metabolite set enrichment analysis showing enrichment ratio of metabolic pathway metabolites. Differential metabolites from cortex of COX 10 KO vs WT and the Small Molecule Pathway Database (SMPDB) were used for this analysis. The enrichment analysis resembles gene set enrichment analysis in transcriptomics. **Panel F:** Metabolite correlation heatmap generated from differential metabolites in cortex of COX 10 KO and WT. Metaboanalyst 5.0 was used for analyses shown in panel B-E and Agilent MassProfiler Professional 15.1 was used for analysis in shown in panel F.

Figure S2 Exemplary MALDI MSI images generated before (A) and after (B) missing value annotation and from reciprocal ratios (C-D). MSI Data was acquired at 80 µm using NEDC as matrix.

Figure S3 Ratio of glutamate to glutamine and Fe^{2+} abundance are co-enriched in the outer cortex of the COX10 KO (right 4 sections) and WT (left 4 sections) brain.

Figure S4 ROIs and UMAP scatter plots generated from non-ratio metabolite data. Panel A-I: Nine segmented ROIs generated UMAP and K-mean clustering analysis corresponding to clustered regions of 1-9. Panel J: Scatterplot of UMAP first 2 components (V1 vs V2) projecting the distribution and similarity of 9 segmented ROIs resulting in a incomplete and inconsistent ROIs among replicates. 5 LPE (Table S3) pixel data was used for UMAP analysis.

Figure S5 ROIs and UMAP scatter plots generated from metabolite ratio data. Panel A-I: Nine segmented ROIs generated UMAP and K-mean clustering analysis corresponding to clustered regions of 1-9. Panel J: Scatterplot of UMAP first 2 components (V1 vs V2) projecting the distribution and similarity of 9 segmented ROIs shows a distinct LPE profile between outer cortex (ROI 3) cortex (ROI 8) and ventral thalamus (ROI 5) striatum region(ROI2). Ratio of 5 LPE (Table S3) pixel data was used for UMAP.

Figure S6 Ratio images of NAA, NAAG and aspartate for UMAP-generated ROIs. Panel A-H: Ratio image of NAA to aspartate in 8 UMAP-segmented ROIs. Panel I-J: Ratio images of NAAG to NAA (I) and NAAG to aspartate in ROI 7 of UAMP segmented ROIs.

Figure S7 Images of NAAG and neurotransmitter related metabolites visualized in UMAP-generated ROI 7. Panel A: NAAG is enriched and elevated in in ROI 7–like region of COX 10 KO brain. Panel B-D: NAA,NAAG and glutamine are elevated in ROI 7 of COX 10 KO brain. Panel E: decreased level of aspartate in ROI 7 of COX10 KO; Panel F: Glutamate shows no change in ROI 7 of COX 10 KO compared to WT.

Figure S8 Pixel-by-pixel correlation of glutamine to glutamate ratio with a compendium of all detected metabolites and ratios exclusively in UMAP-generated ROI 7, comparing WT (A) to COX 10 KO (B) brain.

Only significant correlations with a spearman correlation coefficient of greater than 0.4 were presented in the figure.

Figure S9 UMAP using 5LPE ratios generated ROIs consistent with brain anatomy in two separate experiments with horizonal and sagittal brain sections. Panel A-B: Overlay of nine segmented ROIs generated from UMAP and K-mean clustering analysis in horizonal hemisphere sections (A) and sagittal brain sections (B). Panel C-D: Scatterplot of UMAP first 2 components (V1 vs V2) projecting the distribution and similarity of 9 segmented ROIs in horizonal (C) and sagittal sections (D). See Table S3 for the list of 5 LPEs.

References

1. Shimma S. Mass Spectrometry Imaging. *Mass Spectrom (Tokyo).* 2022;11(1):A0102.
2. Zhang H, Delafield DG, Li L. Mass spectrometry imaging: the rise of spatially resolved single-cell omics. *Nat Methods.* 2023;20(3):327-330.
3. Zhang L, Liang X, Takac T, et al. Spatial proteomics of vesicular trafficking: coupling mass spectrometry and imaging approaches in membrane biology. *Plant Biotechnol J.* 2023;21(2):250-269.
4. Wang J, Zhao J, Nie S, Xie M, Li S. MALDI mass spectrometry in food carbohydrates analysis: A review of recent researches. *Food Chem.* 2023;399:133968.
5. Soudah T, Zoabi A, Margulis K. Desorption electrospray ionization mass spectrometry imaging in discovery and development of novel therapies. *Mass Spectrom Rev.* 2023;42(2):751-778.
6. Sivanesan I, Gopal J, Hasan N, Muthu M. A systematic assessment of matrix-assisted laser desorption/ionization time of flight mass spectrometry (MALDI-TOF MS) application for rapid identification of pathogenic microbes that affect food crops: delivered and future deliverables. *RSC Adv.* 2023;13(25):17297-17314.
7. Roncevic A, Koruga N, Soldo Koruga A, et al. MALDI Imaging Mass Spectrometry of High-Grade Gliomas: A Review of Recent Progress and Future Perspective. *Curr Issues Mol Biol.* 2023;45(2):838-851.
8. Moore JL, Patterson NH, Norris JL, Caprioli RM. Prospective on Imaging Mass Spectrometry in Clinical Diagnostics. *Mol Cell Proteomics.* 2023:100576.
9. Liu J, Hu W, Han Y, Nie H. Recent advances in mass spectrometry imaging of single cells. *Anal Bioanal Chem.* 2023;415(18):4093-4110.
10. Li D, Ouyang Z, Ma X. Mass Spectrometry Imaging for Single-Cell or Subcellular Lipidomics: A Review of Recent Advancements and Future Development. *Molecules.* 2023;28(6).
11. Jiang LX, Yang M, Wali SN, Laskin J. High-Throughput Mass Spectrometry Imaging of Biological Systems: Current Approaches and Future Directions. *Trends Analyt Chem.* 2023;163.
12. Ikegawa M, Kakuda N, Miyasaka T, et al. Mass Spectrometry Imaging in Alzheimer's Disease. *Brain Connect.* 2023.
13. Gorman BL, Torti SV, Torti FM, Anderton CR. Mass spectrometry imaging of metals in tissues and cells: Methods and biological applications. *Biochim Biophys Acta Gen Subj.* 2023:130329.
14. Gitta S, Mark L, Szentpeteri JL, Szabo E. Lipid Changes in the Peri-Implantation Period with Mass Spectrometry Imaging: A Systematic Review. *Life (Basel).* 2023;13(1).
15. Zou Y, Tang W, Li B. Mass spectrometry imaging and its potential in food microbiology. *Int J Food Microbiol.* 2022;371:109675.
16. Zhao Z, Ding Y, Tran LJ, Chai G, Lin L. Innovative breakthroughs facilitated by single-cell multi-omics: manipulating natural killer cell functionality correlates with a novel subcategory of melanoma cells. *Front Immunol.* 2023;14:1196892.
17. Vos DRN, Ellis SR, Balluff B, Heeren RMA. Experimental and Data Analysis Considerations for Three-Dimensional Mass Spectrometry Imaging in Biomedical Research. *Mol Imaging Biol.* 2021;23(2):149-159.
18. Verbeeck N, Caprioli RM, Van de Plas R. Unsupervised machine learning for exploratory data analysis in imaging mass spectrometry. *Mass Spectrom Rev.* 2020;39(3):245-291.
19. Alexandrov T. MALDI imaging mass spectrometry: statistical data analysis and current computational challenges. *BMC Bioinformatics.* 2012;13 Suppl 16(Suppl 16):S11.
20. Trede D, Kobarg JH, Oetjen J, Thiele H, Maass P, Alexandrov T. On the importance of mathematical methods for analysis of MALDI-imaging mass spectrometry data. *J Integr Bioinform.* 2012;9(1):189.
21. Riches SF, Payne GS, Morgan VA, et al. MRI in the detection of prostate cancer: combined apparent diffusion coefficient, metabolite ratio, and vascular parameters. *AJR Am J Roentgenol.* 2009;193(6):1583-1591.

22. Suhre K, Wallaschofski H, Raffler J, et al. A genome-wide association study of metabolic traits in human urine. *Nat Genet.* 2011;43(6):565-569.
23. Illig T, Gieger C, Zhai G, et al. A genome-wide perspective of genetic variation in human metabolism. *Nat Genet.* 2010;42(2):137-141.
24. Gieger C, Geistlinger L, Altmaier E, et al. Genetics meets metabolomics: a genome-wide association study of metabolite profiles in human serum. *PLoS Genet.* 2008;4(11):e1000282.
25. Petersen AK, Krumsiek J, Wagele B, et al. On the hypothesis-free testing of metabolite ratios in genome-wide and metabolome-wide association studies. *BMC Bioinformatics.* 2012;13:120.
26. Lassen JK, Wang T, Nielsen KL, Hasselstrom JB, Johannsen M, Villesen P. Large-Scale metabolomics: Predicting biological age using 10,133 routine untargeted LC-MS measurements. *Aging Cell.* 2023;22(5):e13813.
27. Pang Z, Zhou G, Ewald J, et al. Using MetaboAnalyst 5.0 for LC-HRMS spectra processing, multi-omics integration and covariate adjustment of global metabolomics data. *Nat Protoc.* 2022;17(8):1735-1761.
28. Thompson PT, Moseley HNB. MESSES: Software for Transforming Messy Research Datasets into Clean Submissions to Metabolomics Workbench for Public Sharing. *Metabolites.* 2023;13(7).
29. Powell CD, Moseley HNB. The metabolomics workbench file status website: a metadata repository promoting FAIR principles of metabolomics data. *BMC Bioinformatics.* 2023;24(1):299.
30. Sud M, Fahy E, Cotter D, et al. Metabolomics Workbench: An international repository for metabolomics data and metadata, metabolite standards, protocols, tutorials and training, and analysis tools. *Nucleic Acids Res.* 2016;44(D1):D463-470.
31. Rodeiro J, Vidana-Vila E, Navarro J, Mallol R. CloMet: A Novel Open-Source and Modular Software Platform That Connects Established Metabolomics Repositories and Data Analysis Resources. *J Proteome Res.* 2023;22(8):2540-2547.
32. Du X, Dastmalchi F, Ye H, et al. Evaluating LC-HRMS metabolomics data processing software using FAIR principles for research software. *Metabolomics.* 2023;19(2):11.
33. Dekermanjian J, Labeikovsky W, Ghosh D, Kechris K. MSCAT: A Machine Learning Assisted Catalog of Metabolomics Software Tools. *Metabolites.* 2021;11(10).
34. Plyushchenko IV, Fedorova ES, Potoldykova NV, Polyakovskiy KA, Glukhov AI, Rodin IA. Omics Untargeted Key Script: R-Based Software Toolbox for Untargeted Metabolomics with Bladder Cancer Biomarkers Discovery Case Study. *J Proteome Res.* 2022;21(3):833-847.
35. Misra BB. New software tools, databases, and resources in metabolomics: updates from 2020. *Metabolomics.* 2021;17(5):49.
36. Chang HY, Colby SM, Du X, et al. A Practical Guide to Metabolomics Software Development. *Anal Chem.* 2021;93(4):1912-1923.
37. O'Shea K, Misra BB. Software tools, databases and resources in metabolomics: updates from 2018 to 2019. *Metabolomics.* 2020;16(3):36.
38. Adams KJ, Pratt B, Bose N, et al. Skyline for Small Molecules: A Unifying Software Package for Quantitative Metabolomics. *J Proteome Res.* 2020;19(4):1447-1458.
39. Misra BB. Open-Source Software Tools, Databases, and Resources for Single-Cell and Single-Cell-Type Metabolomics. *Methods Mol Biol.* 2020;2064:191-217.
40. Shahjaman M, Rahman MR, Islam T, Auwul MR, Moni MA, Mollah MNH. rMisbeta: A robust missing value imputation approach in transcriptomics and metabolomics data. *Comput Biol Med.* 2021;138:104911.
41. Wei R, Wang J, Su M, et al. Missing Value Imputation Approach for Mass Spectrometry-based Metabolomics Data. *Sci Rep.* 2018;8(1):663.
42. Jin Z, Kang J, Yu T. Missing value imputation for LC-MS metabolomics data by incorporating metabolic network and adduct ion relations. *Bioinformatics.* 2018;34(9):1555-1561.

43. Di Guida R, Engel J, Allwood JW, et al. Non-targeted UHPLC-MS metabolomic data processing methods: a comparative investigation of normalisation, missing value imputation, transformation and scaling. *Metabolomics.* 2016;12:93.
44. Rieppo J, Hyttinen MM, Jurvelin JS, Helminen HJ. Reference sample method reduces the error caused by variable cryosection thickness in Fourier transform infrared imaging. *Appl Spectrosc.* 2004;58(1):137-140.
45. Wang L, Xu F, Song Z, et al. A high fat diet with a high C18:0/C16:0 ratio induced worse metabolic and transcriptomic profiles in C57BL/6 mice. *Lipids Health Dis.* 2020;19(1):172.
46. Brock TJ, Browse J, Watts JL. Fatty acid desaturation and the regulation of adiposity in Caenorhabditis elegans. *Genetics.* 2007;176(2):865-875.
47. Knecht K, Wiesmuller KH, Gnau V, et al. AMP deaminase in rat brain: localization in neurons and ependymal cells. *J Neurosci Res.* 2001;66(5):941-950.
48. Andruchow ND, Konishi K, Shatenstein B, Bohbot VD. A lower ratio of omega-6 to omega-3 fatty acids predicts better hippocampus-dependent spatial memory and cognitive status in older adults. *Neuropsychology.* 2017;31(7):724-734.
49. Southwell N, Primiano G, Nadkarni V, et al. A coordinated multiorgan metabolic response contributes to human mitochondrial myopathy. *EMBO Mol Med.* 2023;15(7):e16951.
50. Bakker N, Hickey M, Shams R, et al. Oral omega-3 PUFA supplementation modulates inflammation in adipose tissue depots in morbidly obese women: A randomized trial. *Nutrition.* 2023;111:112055.
51. Pinel A, Rigaudiere JP, Morio B, Capel F. Adipose Tissue Dysfunctions in Response to an Obesogenic Diet Are Reduced in Mice after Transgenerational Supplementation with Omega 3 Fatty Acids. *Metabolites.* 2021;11(12).
52. Portela ND, Galvan C, Sanmarco LM, et al. Omega-3-Supplemented Fat Diet Drives Immune Metabolic Response in Visceral Adipose Tissue by Modulating Gut Microbiota in a Mouse Model of Obesity. *Nutrients.* 2023;15(6).
53. Wall R, Ross RP, Shanahan F, et al. Metabolic activity of the enteric microbiota influences the fatty acid composition of murine and porcine liver and adipose tissues. *Am J Clin Nutr.* 2009;89(5):1393-1401.
54. Chiusolo S, Bork CS, Gentile F, et al. Adipose tissue n-3/n-6 fatty acids ratios versus n-3 fatty acids fractions as predictors of myocardial infarction. *Am Heart J.* 2023;262:38-48.
55. Rix TA, Dinesen P, Lundbye-Christensen S, et al. Omega-3 fatty acids in adipose tissue and risk of atrial fibrillation. *Eur J Clin Invest.* 2022;52(1):e13649.
56. Thon M, Hosoi T, Chea C, Ozawa K. Loss of Stearoyl-CoA Desaturase-1 Activity Induced Leptin Resistance in Neuronal Cells. *Biol Pharm Bull.* 2017;40(8):1161-1164.
57. Hertz L, Rothman DL. Glutamine-Glutamate Cycle Flux Is Similar in Cultured Astrocytes and Brain and Both Glutamate Production and Oxidation Are Mainly Catalyzed by Aspartate Aminotransferase. *Biology (Basel).* 2017;6(1).
58. Andersen JV, Schousboe A, Verkhratsky A. Astrocyte energy and neurotransmitter metabolism in Alzheimer's disease: Integration of the glutamate/GABA-glutamine cycle. *Prog Neurobiol.* 2022;217:102331.
59. Pardo B, Rodrigues TB, Contreras L, et al. Brain glutamine synthesis requires neuronal-born aspartate as amino donor for glial glutamate formation. *J Cereb Blood Flow Metab.* 2011;31(1):90-101.
60. Szerb JC, O'Regan PA. Effect of glutamine on glutamate release from hippocampal slices induced by high K+ or by electrical stimulation: interaction with different Ca2+ concentrations. *J Neurochem.* 1985;44(6):1724-1731.
61. Kantorova E, Hnilicova P, Bogner W, et al. Neurocognitive performance in relapsing-remitting multiple sclerosis patients is associated with metabolic abnormalities of the thalamus but not the hippocampus-GABA-edited 1H MRS study. *Neurol Res.* 2022;44(1):57-64.

62. Kantorova E, Hnilicova P, Bogner W, et al. Positivity of oligoclonal bands in the cerebrospinal fluid predisposed to metabolic changes and rearrangement of inhibitory/excitatory neurotransmitters in subcortical brain structures in multiple sclerosis. *Mult Scler Relat Disord.* 2021;52:102978.
63. Limon ID, Angulo-Cruz I, Sanchez-Abdon L, Patricio-Martinez A. Disturbance of the Glutamate-Glutamine Cycle, Secondary to Hepatic Damage, Compromises Memory Function. *Front Neurosci.* 2021;15:578922.
64. Hangel G, Cadrien C, Lazen P, et al. High-resolution metabolic imaging of high-grade gliomas using 7T-CRT-FID-MRSI. *Neuroimage Clin.* 2020;28:102433.
65. Yu J, Guo Y, Sun M, Li B, Zhang Y, Li C. Iron is a potential key mediator of glutamate excitotoxicity in spinal cord motor neurons. *Brain Res.* 2009;1257:102-107.
66. Burger A, Kotze MJ, Stein DJ, Janse van Rensburg S, Howells FM. The relationship between measurement of in vivo brain glutamate and markers of iron metabolism: A proton magnetic resonance spectroscopy study in healthy adults. *Eur J Neurosci.* 2020;51(4):984-990.
67. Peng Yu1, Ming Zhang1,2#, Hui Ding1, Xiaojing Di1, Peng Guan2, Shumin Wang1, Zhenhua Shi1, Dongyun Jiang1,2, Xianglin Duan1,2* and Yan-Zhong Chang1,2. Effect of Glutamate on Brain Iron Metabolism and the Regulation Mechanism. *Journal of Drug Metabolism & Toxicology.* 2015;6(4):1-10.
68. McGahan MC, Harned J, Mukunnemkeril M, Goralska M, Fleisher L, Ferrell JB. Iron alters glutamate secretion by regulating cytosolic aconitase activity. *Am J Physiol Cell Physiol.* 2005;288(5):C1117-1124.
69. Mittal RD, Pandey A, Mittal B, Agarwal KN. Effect of latent iron deficiency on GABA and glutamate neuroreceptors in rat brain. *Indian J Clin Biochem.* 2003;18(1):111-116.
70. Sato T, Shapiro JS, Chang HC, Miller RA, Ardehali H. Aging is associated with increased brain iron through cortex-derived hepcidin expression. *Elife.* 2022;11.
71. Wei S, Shi W, Li M, Gao Q. Calorie restriction down-regulates expression of the iron regulatory hormone hepcidin in normal and D-galactose-induced aging mouse brain. *Rejuvenation Res.* 2014;17(1):19-26.
72. Guo A, Chen Z, Li F, Luo Q. Delineating regions of interest for mass spectrometry imaging by multimodally corroborated spatial segmentation. *Gigascience.* 2022;12.
73. Shi W, Bell S, Iyer H, et al. Integrated silicon microfluidic chip for picoliter-scale analyte segmentation and microscale printing for mass spectrometry imaging. *Lab Chip.* 2022;23(1):72-80.
74. Guo L, Liu X, Zhao C, et al. iSegMSI: An Interactive Strategy to Improve Spatial Segmentation of Mass Spectrometry Imaging Data. *Anal Chem.* 2022;94(42):14522-14529.
75. Zou Y, Tang W, Li B. Spatial segmentation of mass spectrometry imaging data featuring selected principal components. *Talanta.* 2023;253:123958.
76. Baars MJD, Sinha N, Amini M, et al. MATISSE: a method for improved single cell segmentation in imaging mass cytometry. *BMC Biol.* 2021;19(1):99.
77. Guo L, Hu Z, Zhao C, et al. Data Filtering and Its Prioritization in Pipelines for Spatial Segmentation of Mass Spectrometry Imaging. *Anal Chem.* 2021;93(11):4788-4793.
78. Hu H, Yin R, Brown HM, Laskin J. Spatial Segmentation of Mass Spectrometry Imaging Data by Combining Multivariate Clustering and Univariate Thresholding. *Anal Chem.* 2021;93(7):3477-3485.
79. Rothman DL, Behar KL, Prichard JW, Petroff OA. Homocarnosine and the measurement of neuronal pH in patients with epilepsy. *Magn Reson Med.* 1997;38(6):924-929.
80. Filipovic D, Ivetic V, Bozic K, Nikolic V, Naumovic N. [The effect of homocarnosine on neuronal activity during satiation and starvation]. *Med Pregl.* 1993;46(11-12):393-397.
81. Bondarenko TI, Krichevskaia AA, Koshchii GN. [Homocarnosine in the brain of rats during cold adaptation]. *Fiziol Zh SSSR Im I M Sechenova.* 1985;71(3):333-336.
82. Kukharenko RI, Reva AD, Rodina SL. [An increase in the brain homocarnosine level during alcohol intoxication]. *Ukr Biokhim Zh (1978).* 1990;62(1):92-94.
83. Palfreyman MG, Huot S, Grove J. Total GABA and homocarnosine in CSF as indices of brain GABA concentrations. *Neurosci Lett.* 1983;35(2):161-166.

84. Jalil MA, Begum L, Contreras L, et al. Reduced N-acetylaspartate levels in mice lacking aralar, a brain- and muscle-type mitochondrial aspartate-glutamate carrier. *J Biol Chem.* 2005;280(35):31333-31339.
85. Ohtsuka C, Takahashi H. Brain function estimated from the ratio of glutamine to homocarnosine levels in cerebrospinal fluid. *Brain Dev.* 1983;5(5):509-511.
86. Enwonwu CO, Worthington BS. Accumulation of histidine, 3-methylhistidine, and homocarnosine in the brains of protein-calorie deficient monkeys. *J Neurochem.* 1973;21(4):799-807.
87. Rather AA, Chachoo MA. Robust correlation estimation and UMAP assisted topological analysis of omics data for disease subtyping. *Comput Biol Med.* 2023;155:106640.
88. ElKarami B, Alkhateeb A, Qattous H, Alshomali L, Shahrrava B. Multi-omics Data Integration Model Based on UMAP Embedding and Convolutional Neural Network. *Cancer Inform.* 2022;21:11769351221124205.
89. Do VH, Canzar S. A generalization of t-SNE and UMAP to single-cell multimodal omics. *Genome Biol.* 2021;22(1):130.
90. Dall'Olio L, Bolognesi M, Borghesi S, Cattoretti G, Castellani G. BRAQUE: Bayesian Reduction for Amplified Quantization in UMAP Embedding. *Entropy (Basel).* 2023;25(2).
91. Gare S, Chel S, Abhinav TK, Dhyani V, Jana S, Giri L. Mapping of structural arrangement of cells and collective calcium transients: an integrated framework combining live cell imaging using confocal microscopy and UMAP-assisted HDBSCAN-based approach. *Integr Biol (Camb).* 2022;14(8-12):184-203.
92. Stolarek I, Samelak-Czajka A, Figlerowicz M, Jackowiak P. Dimensionality reduction by UMAP for visualizing and aiding in classification of imaging flow cytometry data. *iScience.* 2022;25(10):105142.
93. Vermeulen M, Smith K, Eremin K, Rayner G, Walton M. Application of Uniform Manifold Approximation and Projection (UMAP) in spectral imaging of artworks. *Spectrochim Acta A Mol Biomol Spectrosc.* 2021;252:119547.
94. Kharel P, Singhal NK, Mahendran T, et al. NAT8L mRNA oxidation is linked to neurodegeneration in multiple sclerosis. *Cell Chem Biol.* 2023;30(3):308-320 e305.
95. Uno K, Miyanishi H, Sodeyama K, et al. Vulnerability to depressive behavior induced by overexpression of striatal Shati/Nat8l via the serotonergic neuronal pathway in mice. *Behav Brain Res.* 2019;376:112227.
96. Morland C, Nordengen K. N-Acetyl-Aspartyl-Glutamate in Brain Health and Disease. *Int J Mol Sci.* 2022;23(3).
97. Zizzo MG, Mule F, Serio R. Evidence that ATP or a related purine is an excitatory neurotransmitter in the longitudinal muscle of mouse distal colon. *Br J Pharmacol.* 2007;151(1):73-81.
98. Mutafova-Yambolieva VN, Durnin L. The purinergic neurotransmitter revisited: a single substance or multiple players? *Pharmacol Ther.* 2014;144(2):162-191.
99. Goyal RK. Evidence for beta-nicotinamide adenine dinucleotide as a purinergic, inhibitory neurotransmitter in doubt. *Gastroenterology.* 2011;141(4):e27; author reply e27-28.
100. Jimenez E, Zafra F, Perez-Sen R, et al. P2Y purinergic regulation of the glycine neurotransmitter transporters. *J Biol Chem.* 2011;286(12):10712-10724.
101. Ribeiro JA. Purinergic inhibition of neurotransmitter release in the central nervous system. *Pharmacol Toxicol.* 1995;77(5):299-305.
102. Tanaka K, Farooqui AA, Siddiqi NJ, Alhomida AS, Ong WY. Effects of docosahexaenoic Acid on neurotransmission. *Biomol Ther (Seoul).* 2012;20(2):152-157.
103. Fuente-Martin E, Garcia-Caceres C, Granado M, et al. Leptin regulates glutamate and glucose transporters in hypothalamic astrocytes. *J Clin Invest.* 2012;122(11):3900-3913.
104. Naranjo V, Contreras A, Merino B, et al. Specific Deletion of the Astrocyte Leptin Receptor Induces Changes in Hippocampus Glutamate Metabolism, Synaptic Transmission and Plasticity. *Neuroscience.* 2020;447:182-190.
105. Xu Y, Kim ER, Zhao R, Myers MG, Jr., Munzberg H, Tong Q. Glutamate release mediates leptin action on energy expenditure. *Mol Metab.* 2013;2(2):109-115.

106. Turnbull MJ, Slater P. Further studies on homocarnosine induced hypothermia. *Life Sci I.* 1970;9(2):83-89.
107. Yoshimatsu H. Hypothalamic neuronal histamine regulates body weight through the modulation of diurnal feeding rhythm. *Nutrition.* 2008;24(9):827-831.

Figure 1

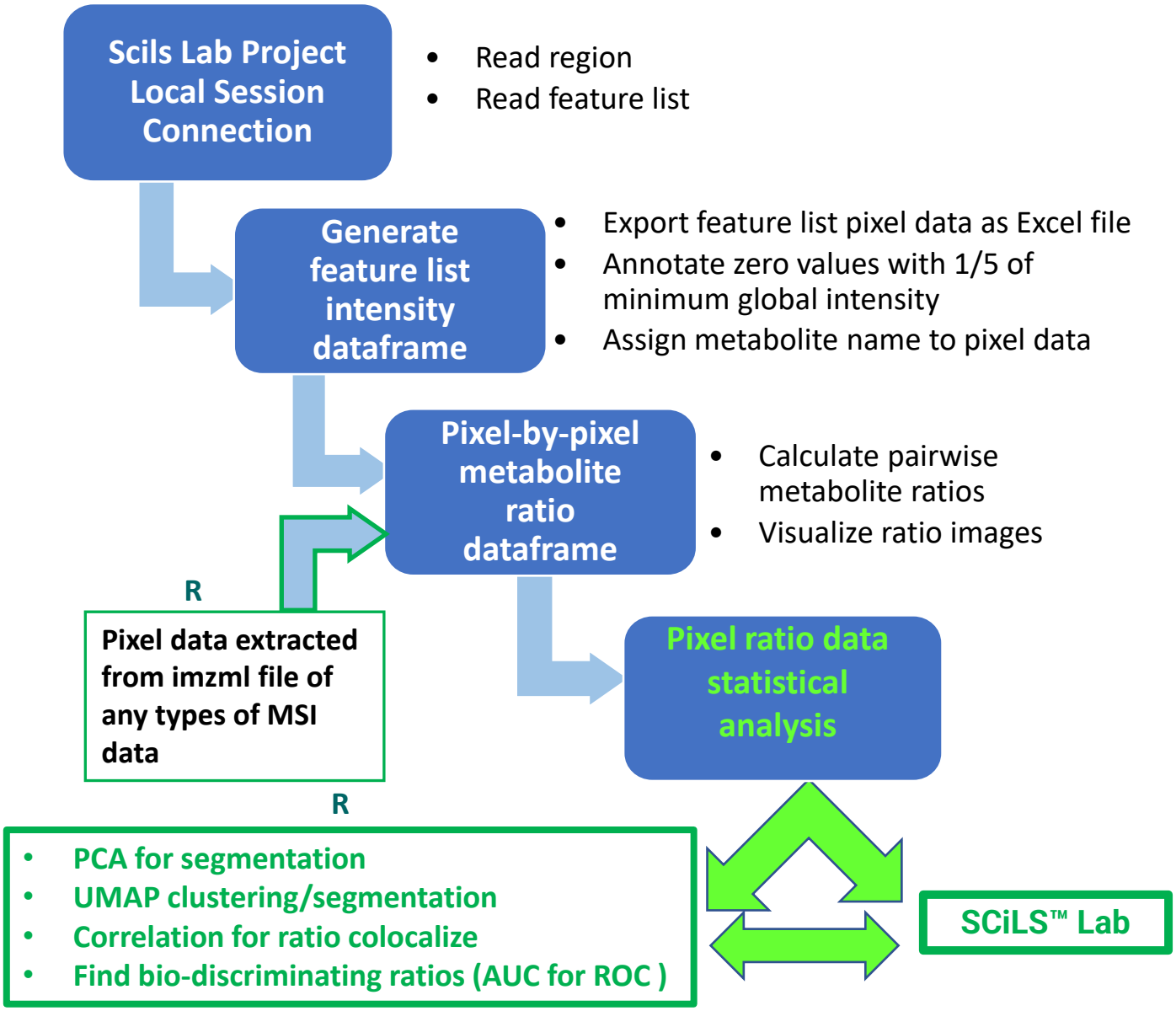
Scils Lab Project Local Session Connection
Read region
Read feature list
Generate feature list intensity dataframe
Export feature list pixel data as Excel file
Annotate zero values with 1/5 of minimum global intensity
Assign metabolite name to pixel data
Pixel-by-pixel metabolite ratio dataframe
Calculate pairwise metabolite ratios
Visualize ratio images
R
Pixel data extracted from imzml file of any types of MSI data
Pixel ratio data statistical analysis
R
PCA for segmentation
UMAP clustering/segmentation
Correlation for ratio colocalize
Find bio-discriminating ratios (AUC for ROC)
SCiLS™ Lab

Figure 2

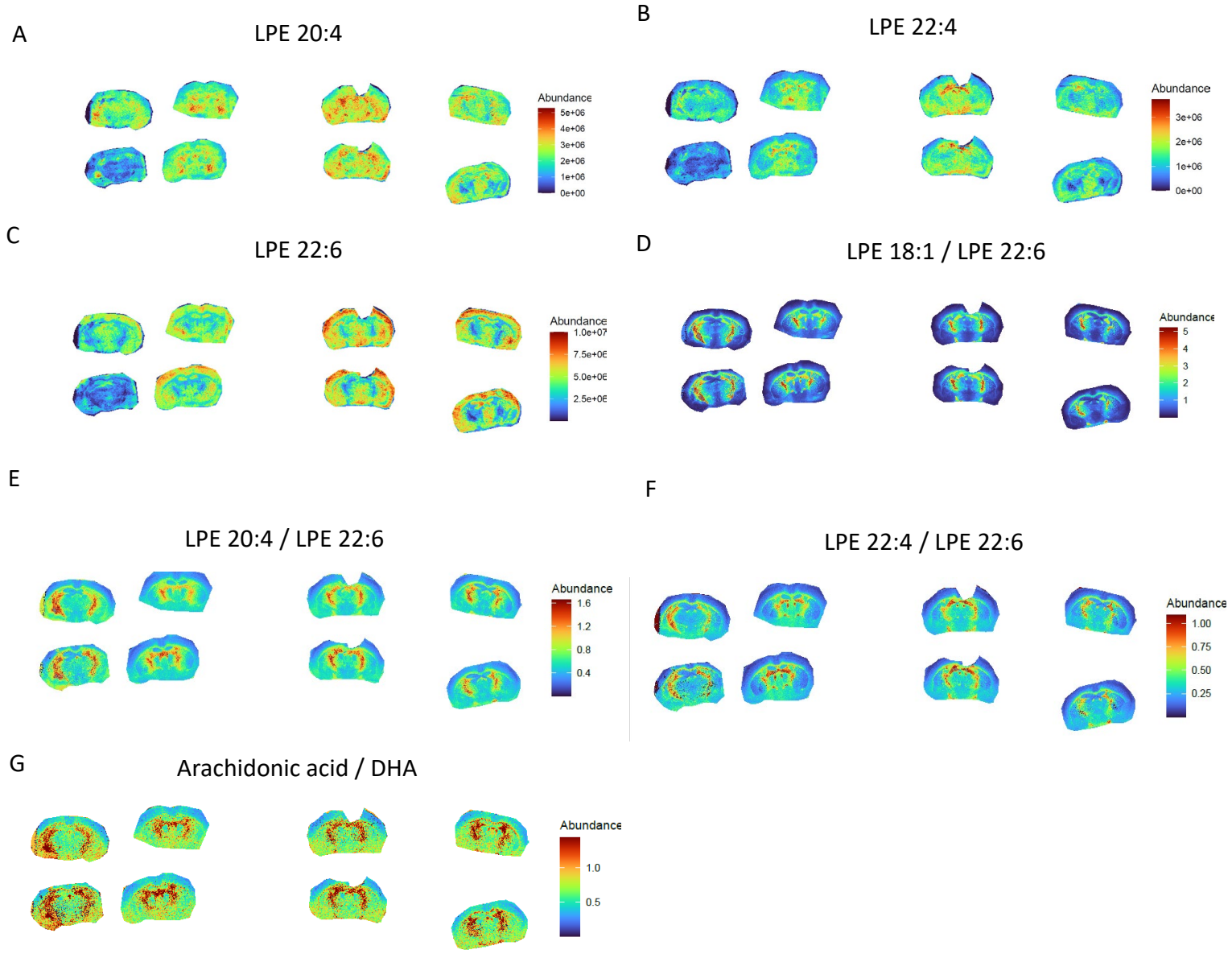
A
LPE 20:4
Abundance
5e+06
4e+06
3e+06
2e+06
1e+06
0e+00
B
LPE 22:4
Abundance
3e+06
2e+06
1e+06
0e+00
C
LPE 22:6
Abundance
1.0e+07
7.5e+06
5.0e+06
2.5e+06
D
LPE 18:1 / LPE 22:6
Abundance
5
4
3
2
1
E
LPE 20:4 / LPE 22:6
Abundance
1.6
1.2
0.8
0.4
F
LPE 22:4 / LPE 22:6
Abundance
1.00
0.75
0.50
0.25
G
Arachidonic acid / DHA
Abundance
1.0
0.5

Figure 3

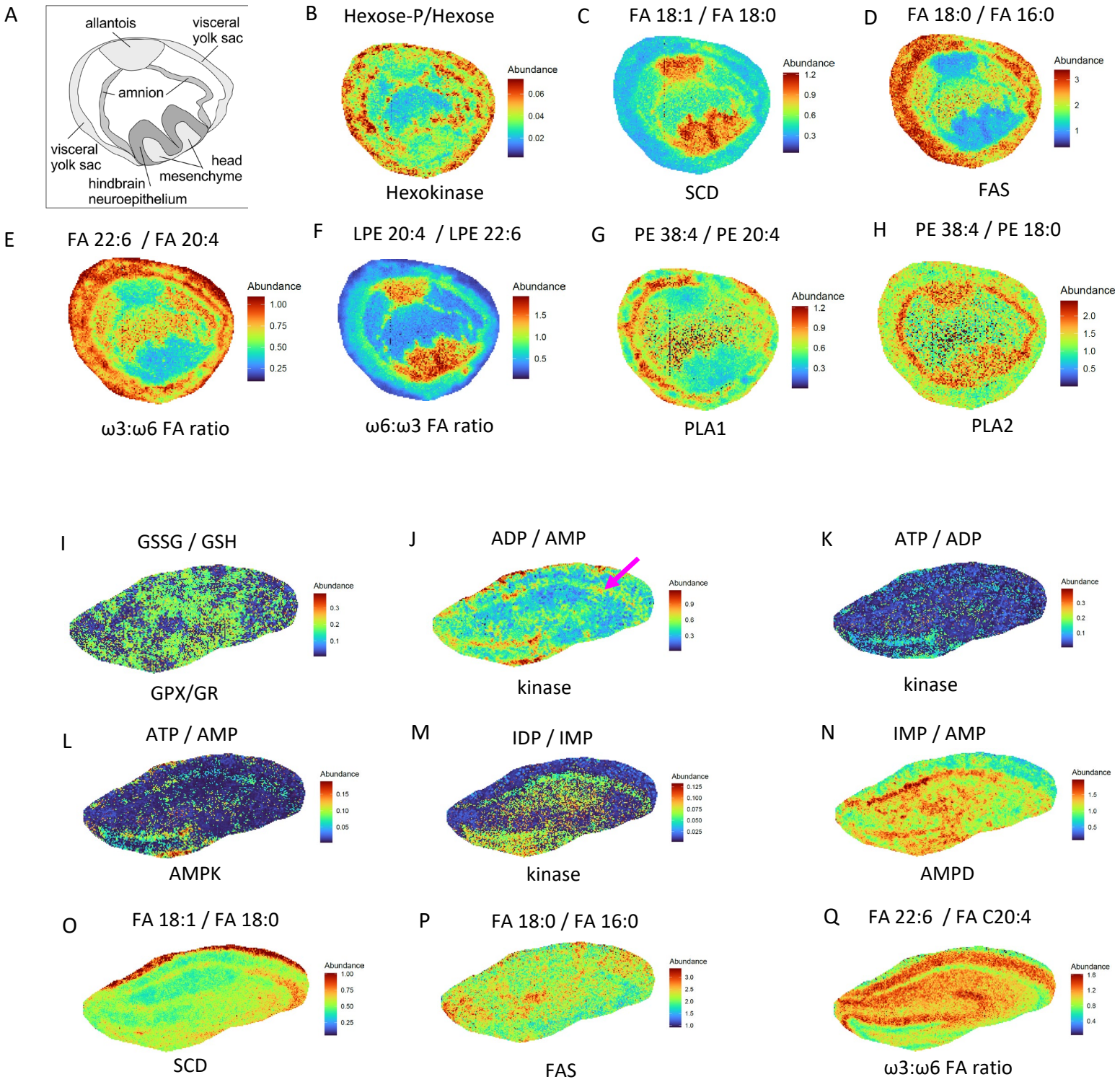
A
allantois
visceral yolk sac
amnion
visceral yolk sac
head mesenchyme
hindbrain neuroepithelium
B
Hexose-P/Hexose
Abundance
0.06
0.04
0.02
Hexokinase
C
FA 18:1 / FA 18:0
Abundance
1.2
0.9
0.6
0.3
SCD
D
FA 18:0 / FA 16:0
Abundance
3
2
1
FAS
E
FA 22:6 / FA 20:4
Abundance
1.00
0.75
0.50
0.25
ω3:ω6 FA ratio
F
LPE 20:4 / LPE 22:6
Abundance
1.5
1.0
0.5
ω6:ω3 FA ratio
G
PE 38:4 / PE 20:4
Abundance
1.2
0.9
0.6
0.3
PLA1
H
PE 38:4 / PE 18:0
Abundance
2.0
1.5
1.0
0.5
PLA2
I
GSSG / GSH
Abundance
0.3
0.2
0.1
GPX/GR
J
ADP / AMP
Abundance
0.9
0.6
0.3
kinase
K
ATP / ADP
Abundance
0.3
0.2
0.1
kinase
L
ATP / AMP
Abundance
0.15
0.10
0.05
AMPK
M
IDP / IMP
Abundance
0.125
0.100
0.075
0.050
0.025
kinase
N
IMP / AMP
Abundance
1.5
1.0
0.5
AMPD
O
FA 18:1 / FA 18:0
Abundance
1.00
0.75
0.50
0.25
SCD
P
FA 18:0 / FA 16:0
Abundance
3.0
2.5
2.0
1.5
1.0
FAS
Q
FA 22:6 / FA C20:4
Abundance
1.6
1.2
0.8
0.4
ω3:ω6 FA ratio

Figure 4

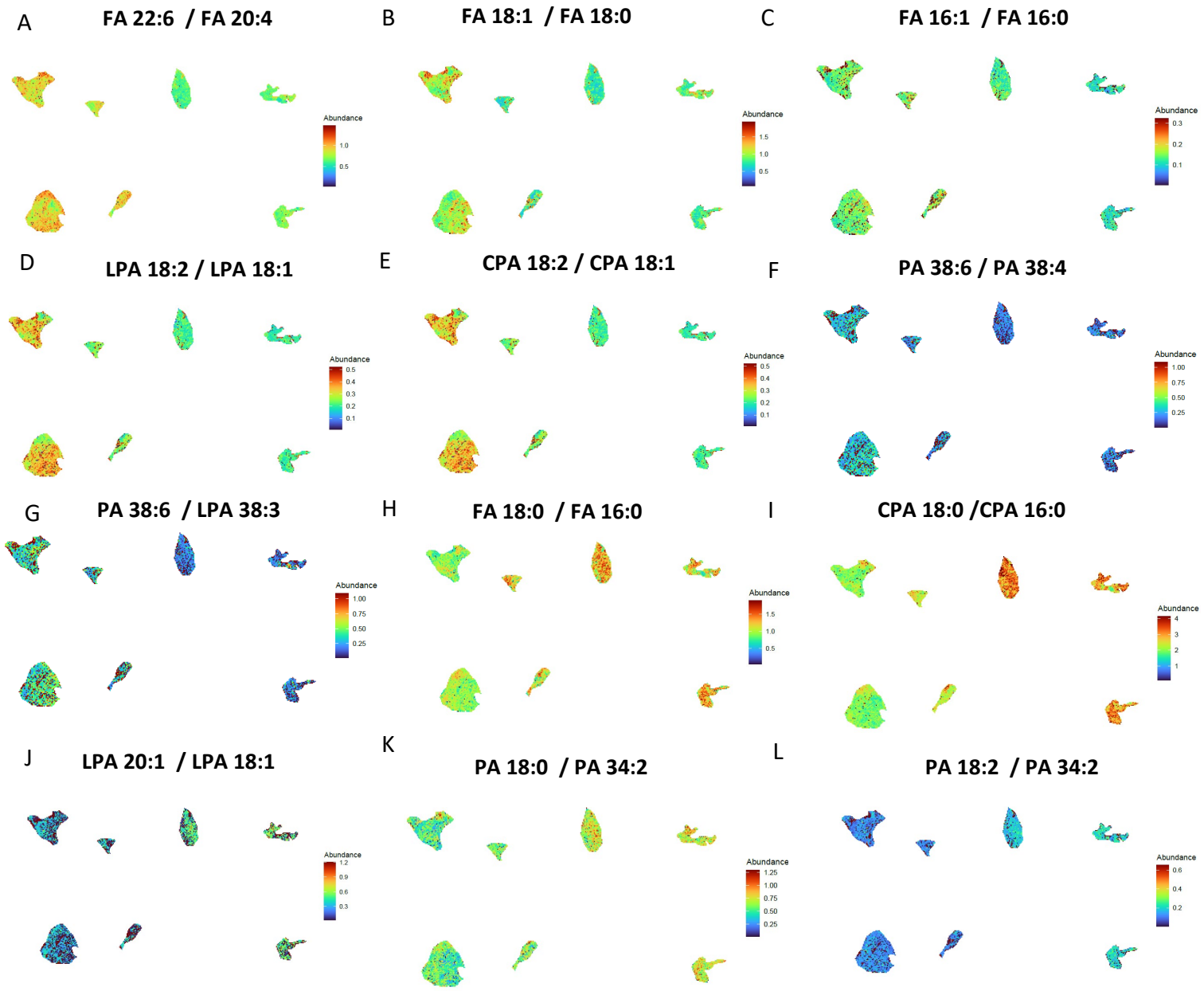
A
FA 22:6 / FA 20:4
Abundance
1.0
0.5
B
FA 18:1 / FA 18:0
Abundance
1.5
1.0
0.5
C
FA 16:1 / FA 16:0
Abundance
0.3
0.2
0.1
D
LPA 18:2 / LPA 18:1
Abundance
0.5
0.4
0.3
0.2
0.1
E
CPA 18:2 / CPA 18:1
Abundance
0.5
0.4
0.3
0.2
0.1
F
PA 38:6 / PA 38:4
Abundance
1.00
0.75
0.50
0.25
G
PA 38:6 / LPA 38:3
Abundance
1.00
0.75
0.50
0.25
H
FA 18:0 / FA 16:0
Abundance
1.5
1.0
0.5
I
CPA 18:0 /CPA 16:0
Abundance
4
3
2
1
J
LPA 20:1 / LPA 18:1
Abundance
1.2
0.9
0.6
0.3
K
PA 18:0 / PA 34:2
Abundance
1.25
1.00
0.75
0.50
0.25
L
PA 18:2 / PA 34:2
Abundance
0.6
0.4
0.2

Figure 5

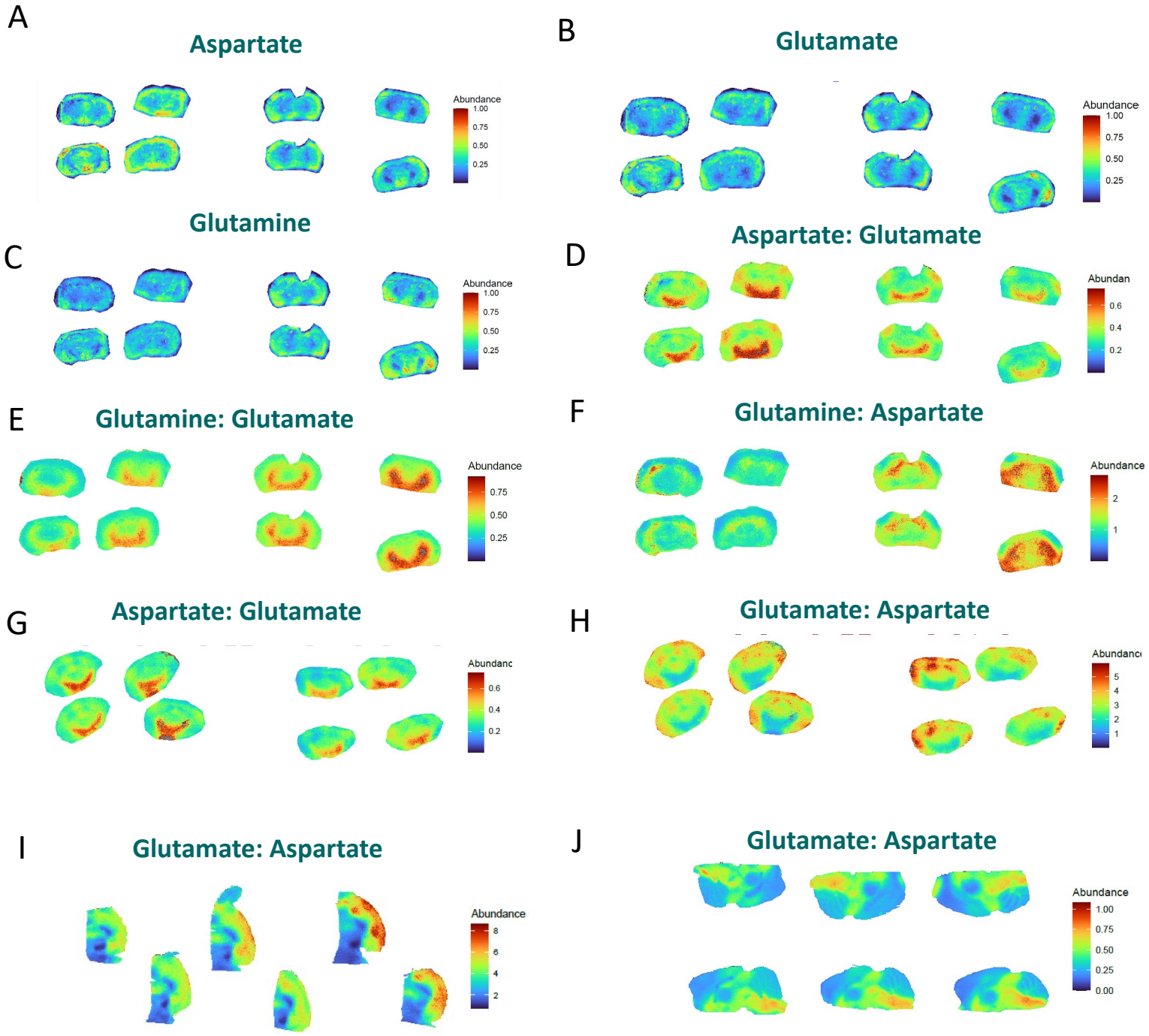
A
Aspartate
Abundance
1.00
0.75
0.50
0.25
B
Glutamate
Abundance
1.00
0.75
0.50
0.25
C
Glutamine
Abundance
1.00
0.75
0.50
0.25
D
Aspartate: Glutamate
Abundan
0.6
0.4
0.2
E
Glutamine: Glutamate
Abundance
0.75
0.50
0.25
F
Glutamine: Aspartate
Abundance
2
1
G
Aspartate: Glutamate
Abundanc
0.6
0.4
0.2
H
Glutamate: Aspartate
Abundanc
5
4
3
2
1
I
Glutamate: Aspartate
Abundance
8
6
4
2
J
Glutamate: Aspartate
Abundance
1.00
0.75
0.50
0.25
0.00

Figure 6

A **10 Glutamate Metabolites**

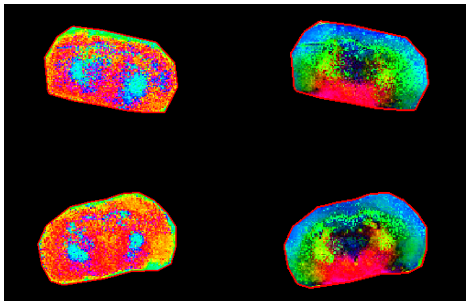

B **5 phospholipids (-PEs)**

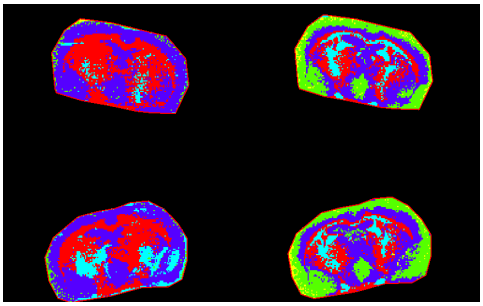

Ratio: **-** **+** **-** **+**

Figure 7

A

Asp :Gln

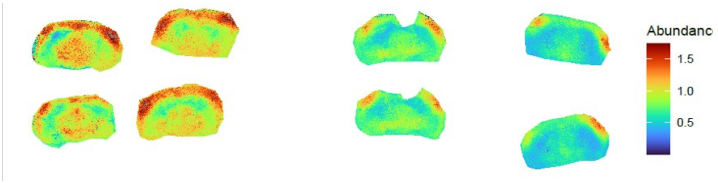

B

Homocarnosine: Asp

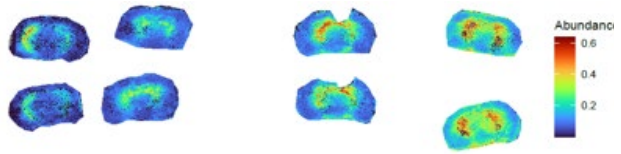

C

Homocarnosine: Gln

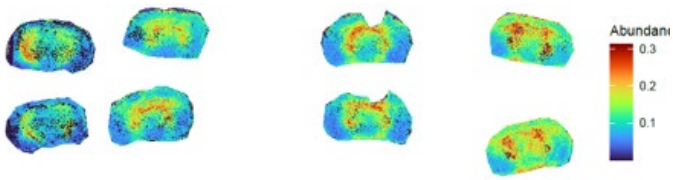

D

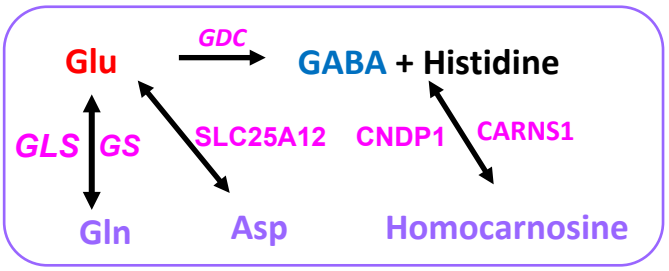

Homocarnosine

E

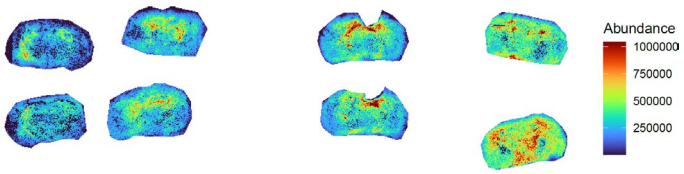

F

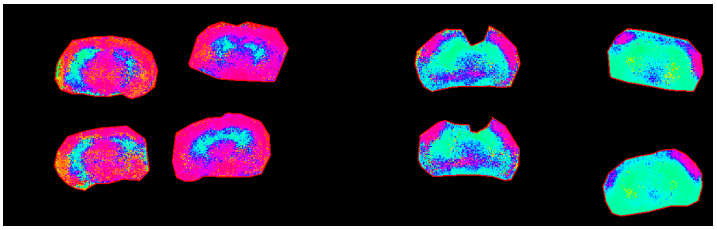

G

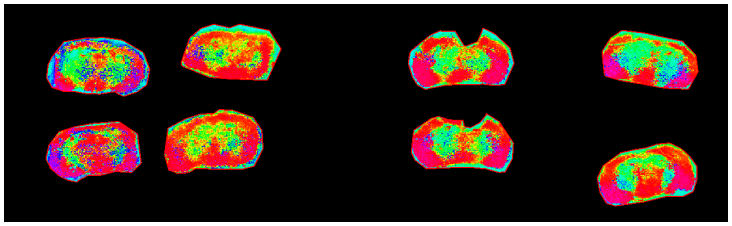

Figure 8

A

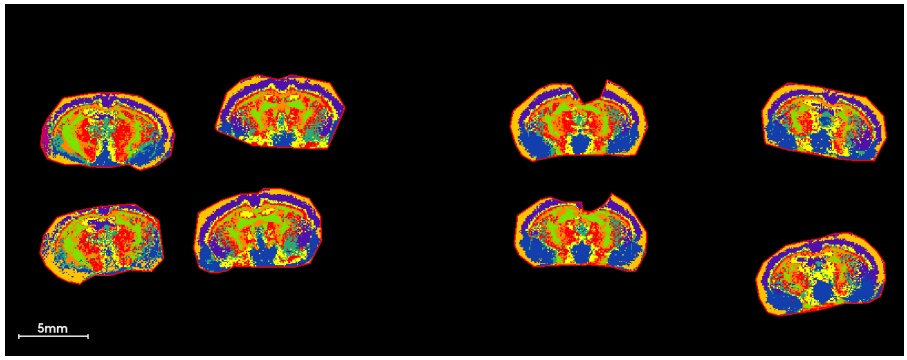

B

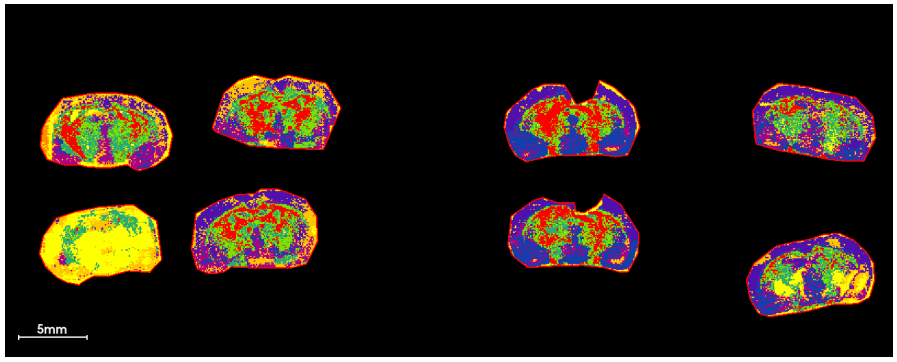

Figure S1

A

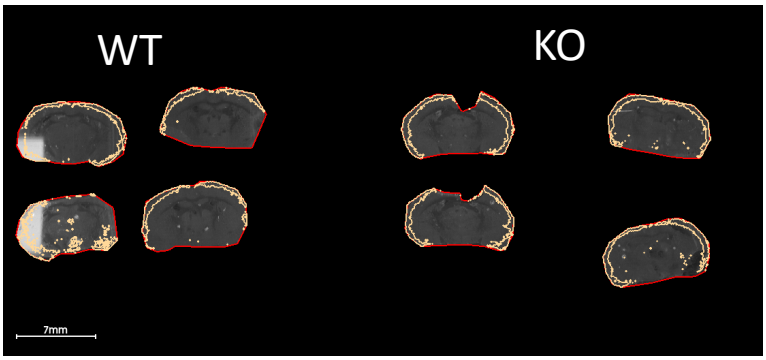

B

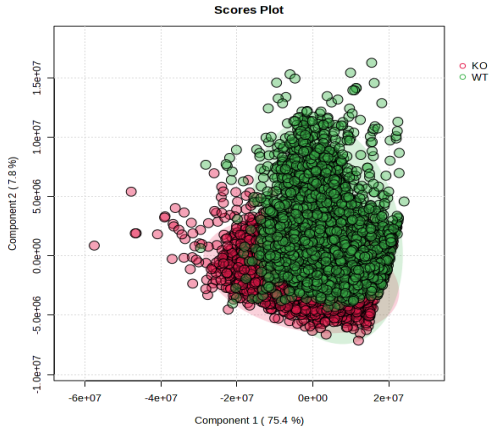

C

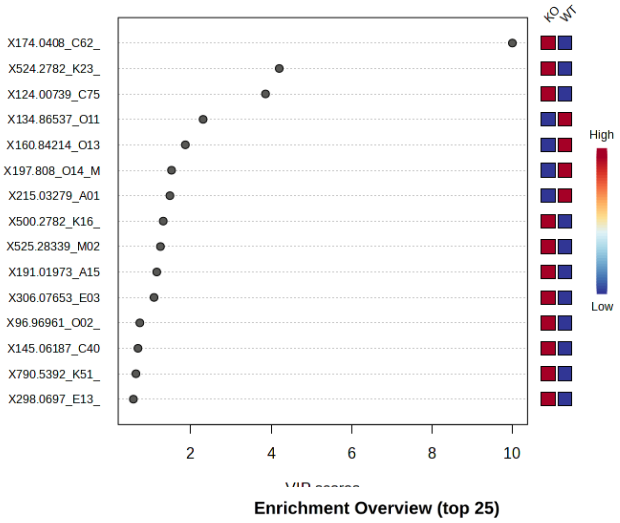

D

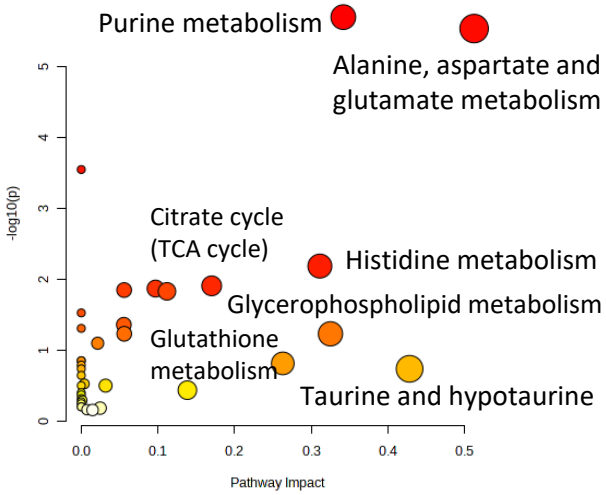

E

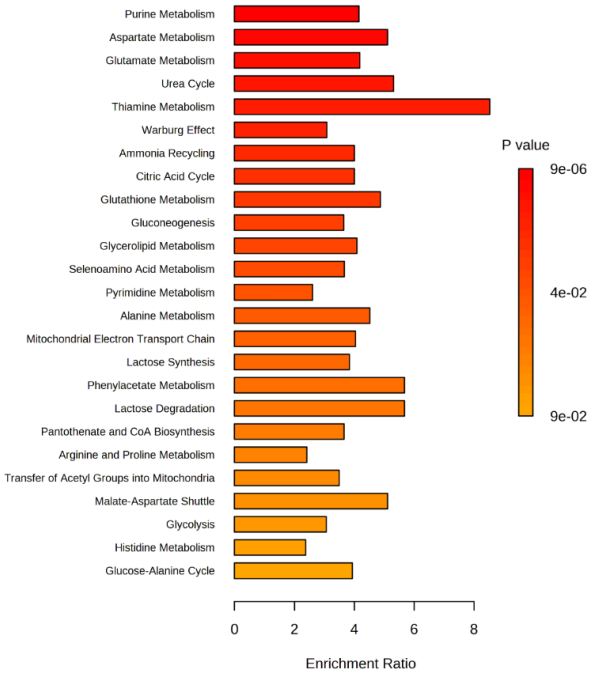

F

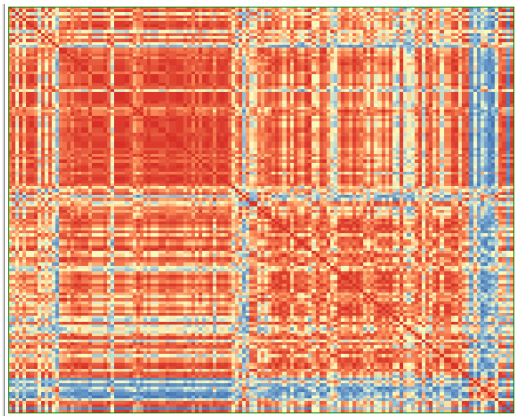

Figure S2

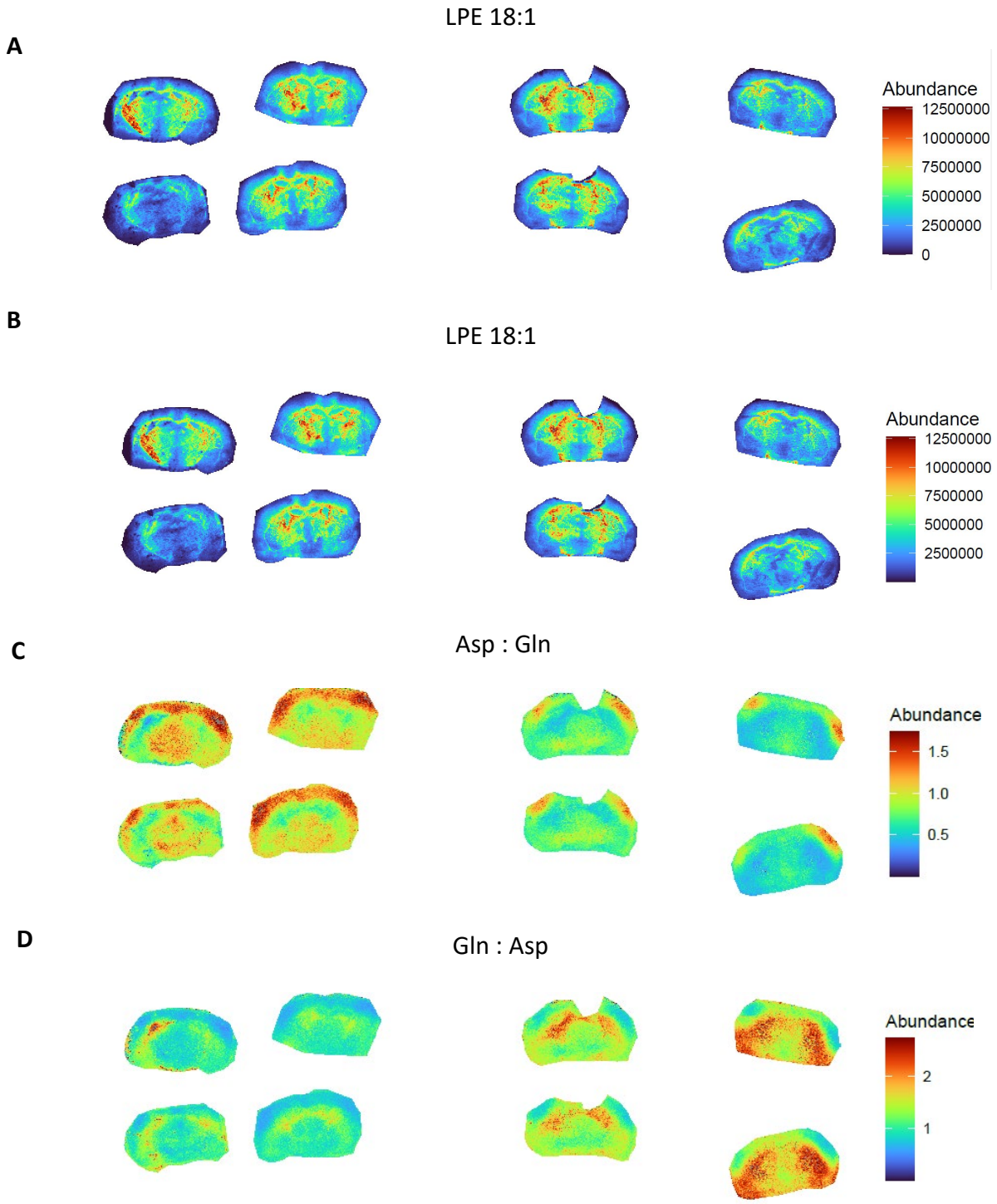
A
LPE 18:1
Abundance
12500000
10000000
7500000
5000000
2500000
0
B
LPE 18:1
Abundance
12500000
10000000
7500000
5000000
2500000
C
Asp : Gln
Abundance
1.5
1.0
0.5
D
Gln : Asp
Abundance
2
1

Figure S3

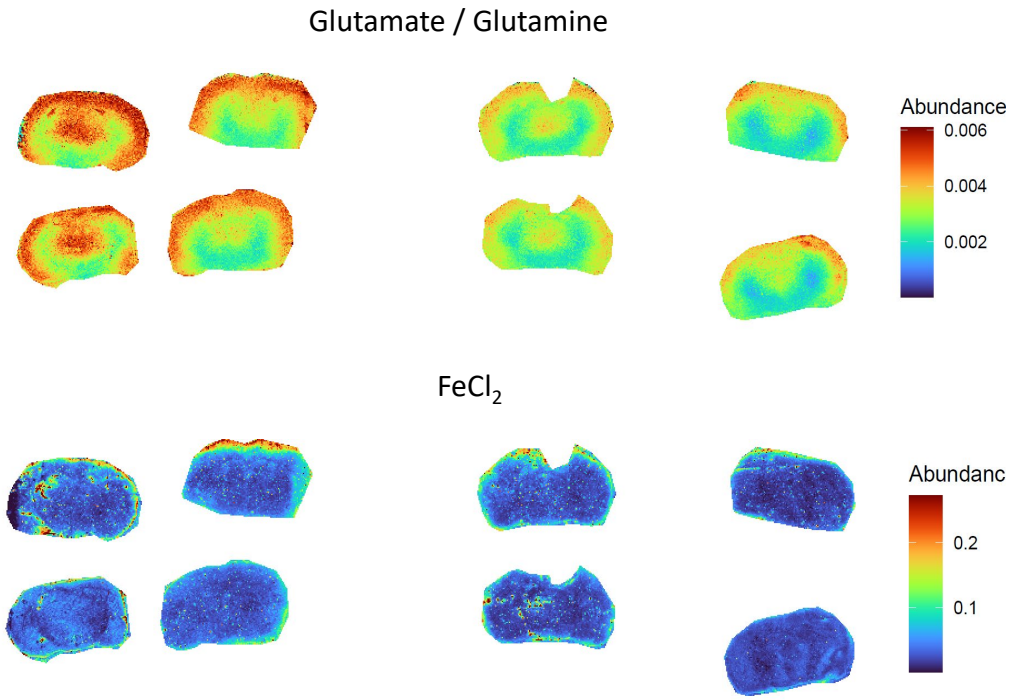
Glutamate / Glutamine
Abundance
0.006
0.004
0.002
FeCl2
Abundanc
0.2
0.1

Figure S4

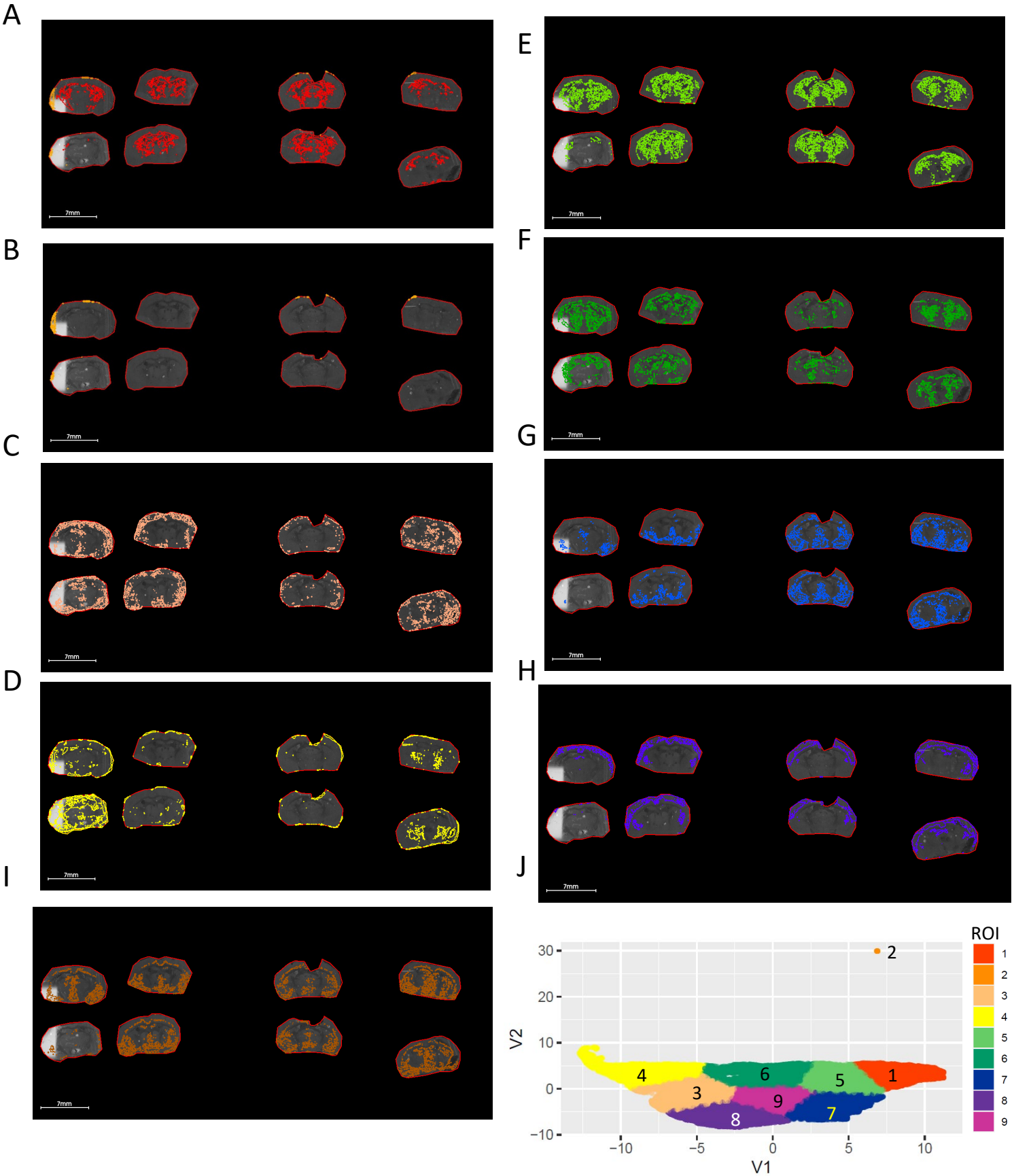

Figure S5

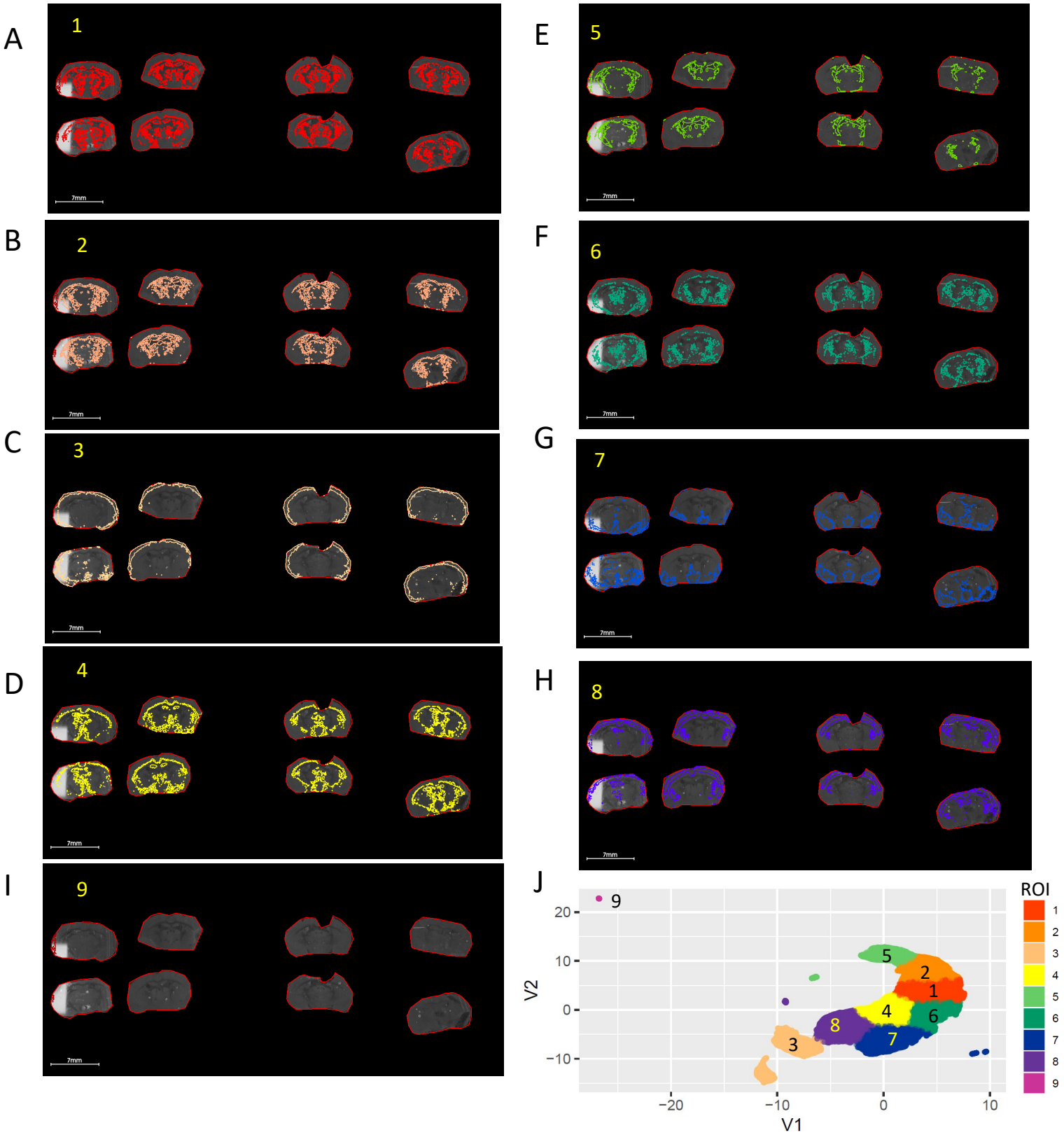

Figure S6

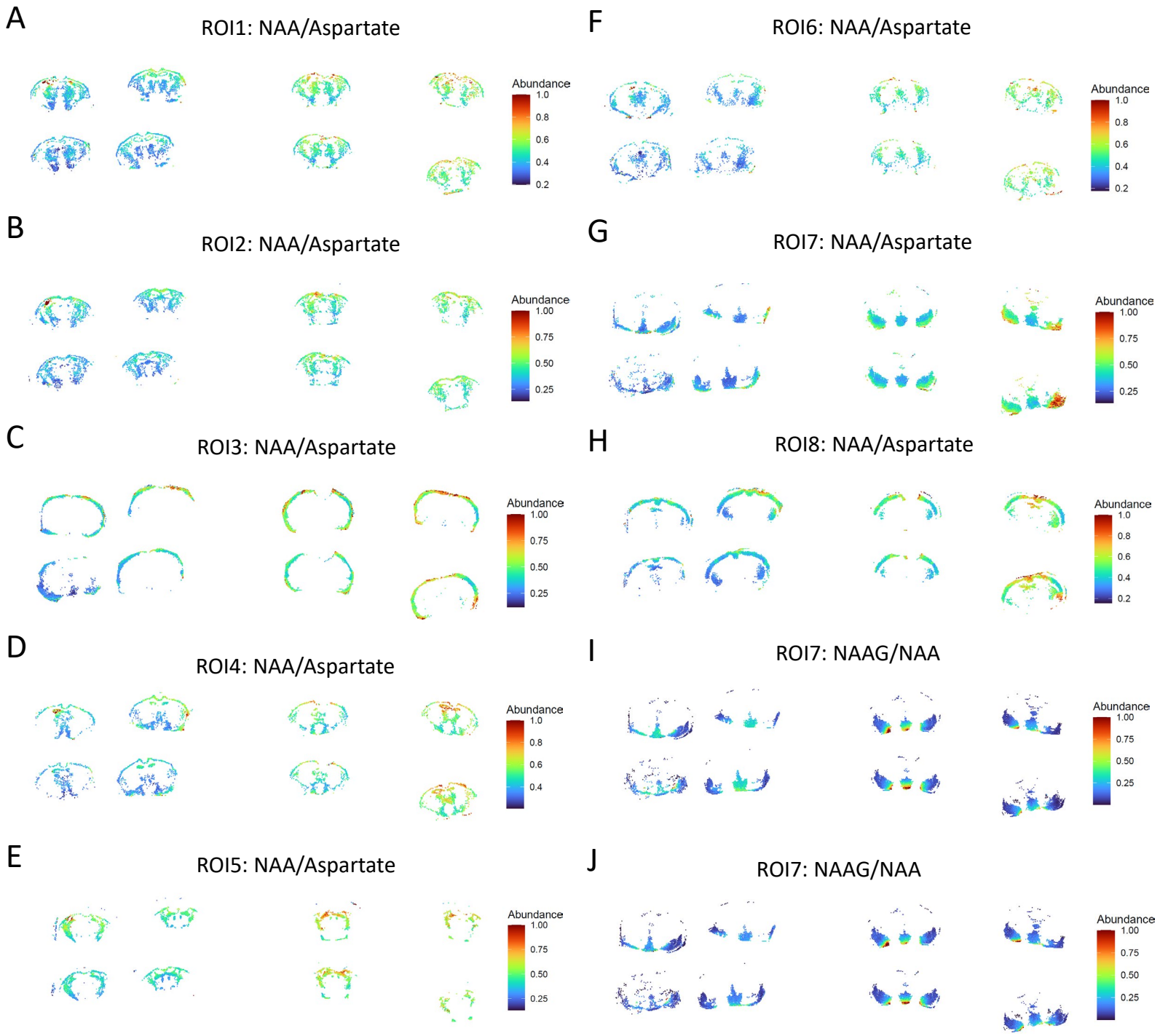
A
ROI1: NAA/Aspartate
Abundance
1.0
0.8
0.6
0.4
0.2
B
ROI2: NAA/Aspartate
Abundance
1.00
0.75
0.50
0.25
C
ROI3: NAA/Aspartate
Abundance
1.00
0.75
0.50
0.25
D
ROI4: NAA/Aspartate
Abundance
1.0
0.8
0.6
0.4
E
ROI5: NAA/Aspartate
Abundance
1.00
0.75
0.50
0.25
F
ROI6: NAA/Aspartate
Abundance
1.0
0.8
0.6
0.4
0.2
G
ROI7: NAA/Aspartate
Abundance
1.00
0.75
0.50
0.25
H
ROI8: NAA/Aspartate
Abundance
1.0
0.8
0.6
0.4
0.2
I
ROI7: NAAG/NAA
Abundance
1.00
0.75
0.50
0.25
J
ROI7: NAAG/NAA
Abundance
1.00
0.75
0.50
0.25

Figure S7

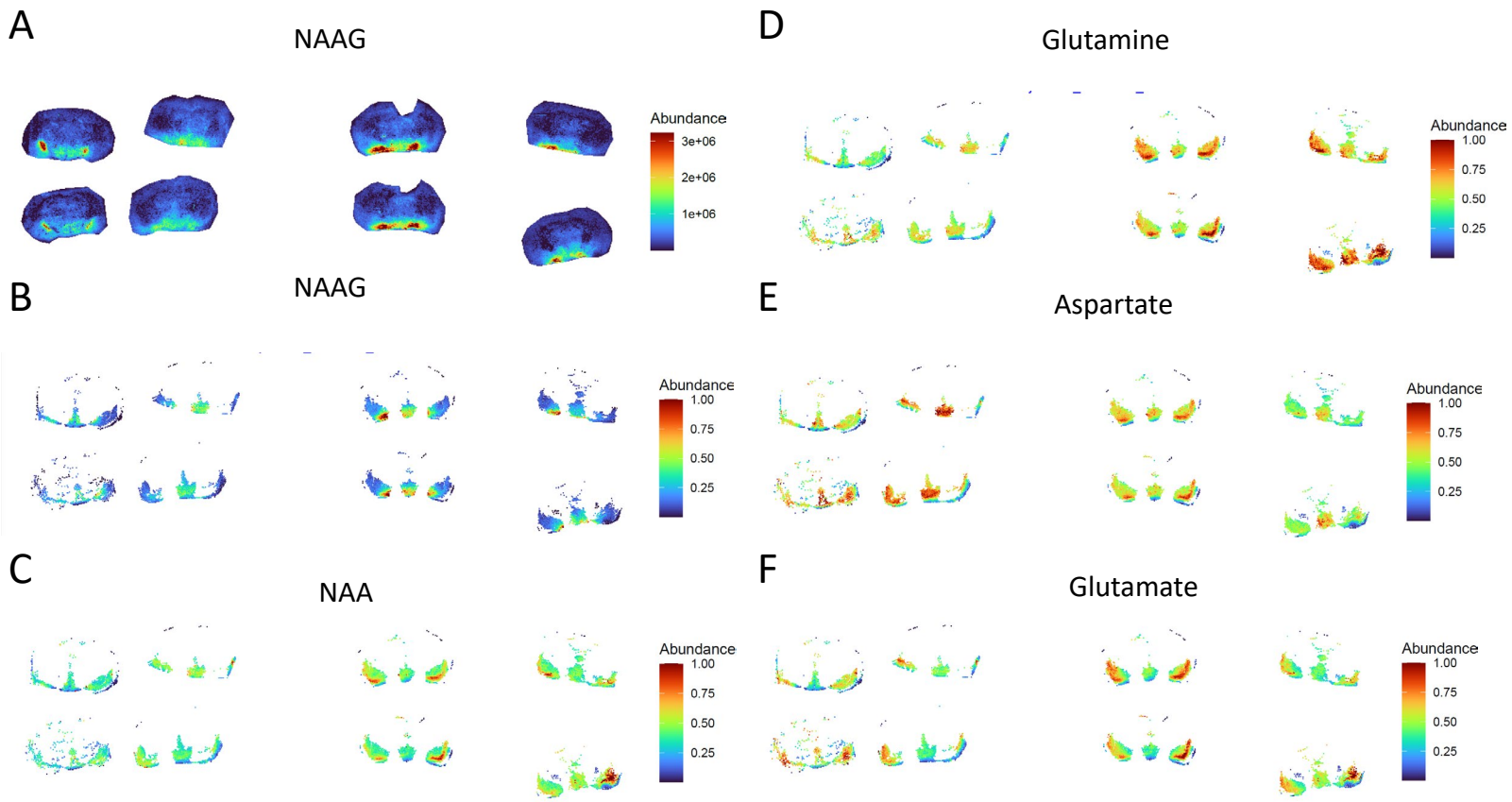
A
NAAG
Abundance
3e+06
2e+06
1e+06
B
NAAG
Abundance
1.00
0.75
0.50
0.25
C
NAA
Abundance
1.00
0.75
0.50
0.25
D
Glutamine
Abundance
1.00
0.75
0.50
0.25
E
Aspartate
Abundance
1.00
0.75
0.50
0.25
F
Glutamate
Abundance
1.00
0.75
0.50
0.25

Figure S8

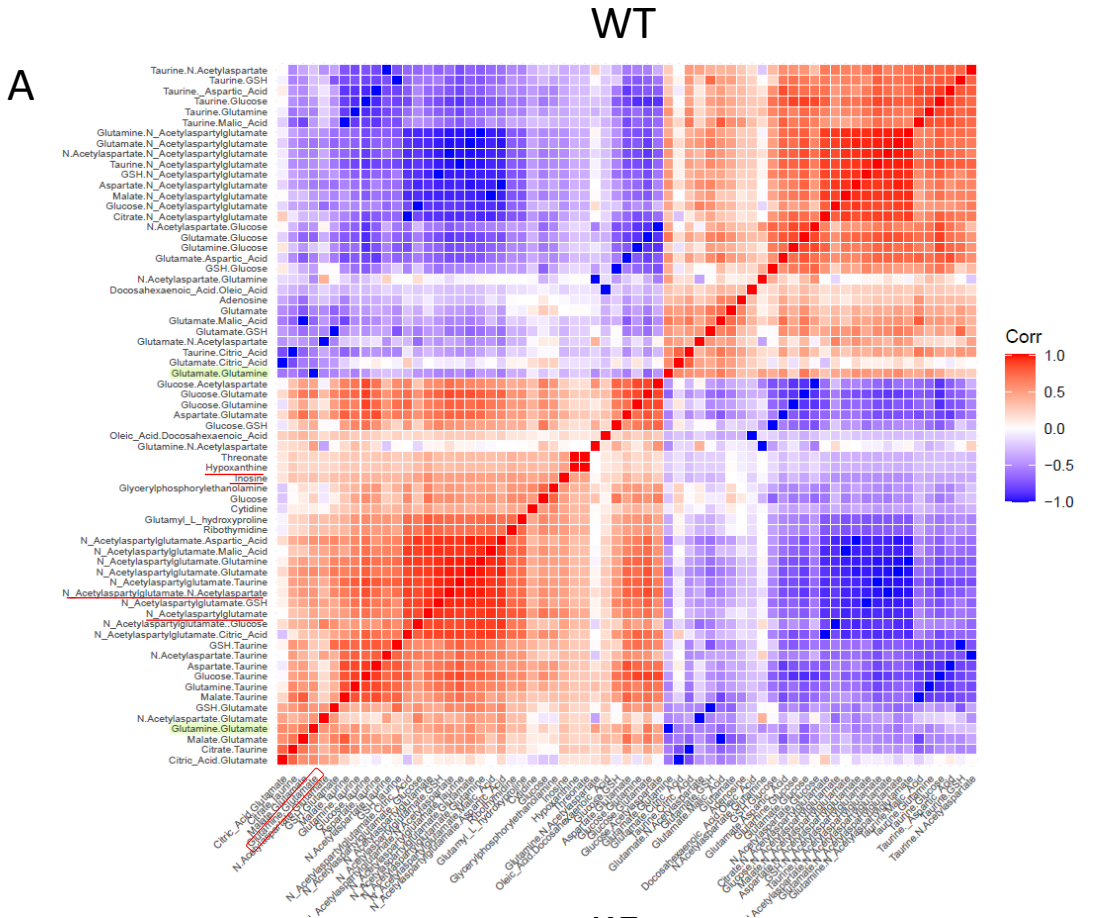

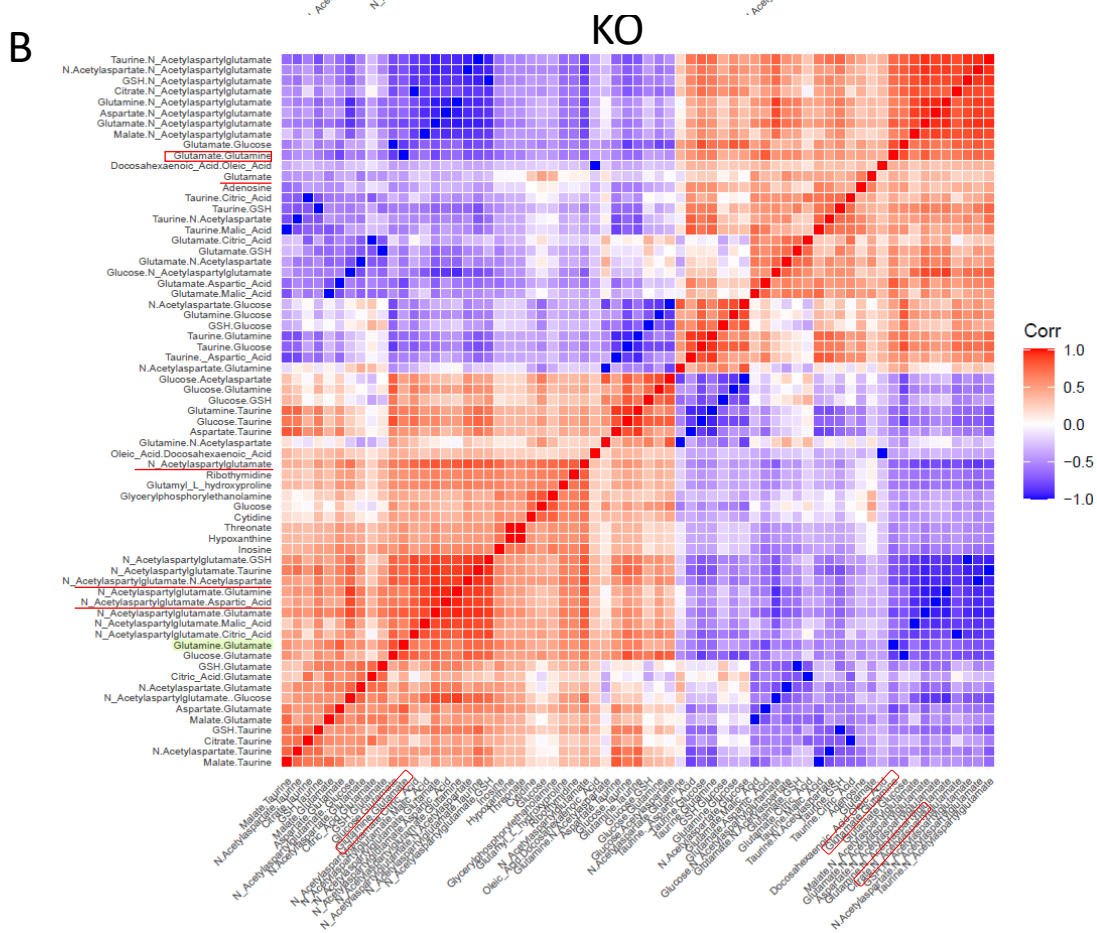

Fig S9

A

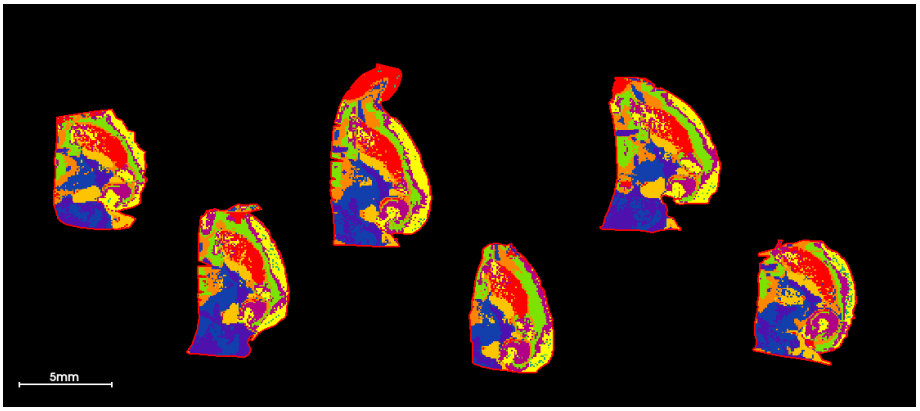
5mm

B

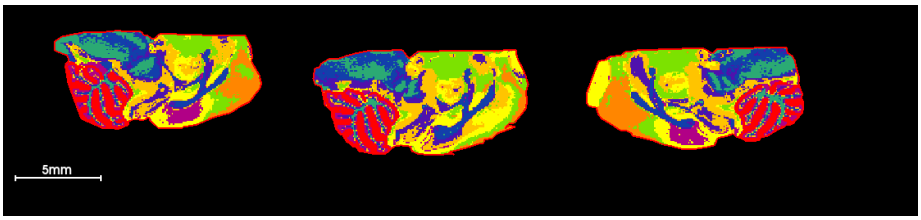
5mm

C

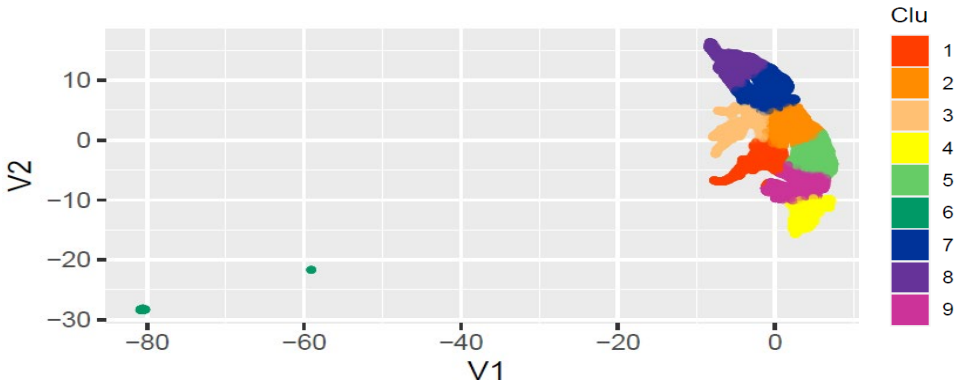
Clu
1
2
3
4
5
6
7
8
9
V2
10
0
−10
−20
−30
−80
−60
−40
−20
0
V1

D

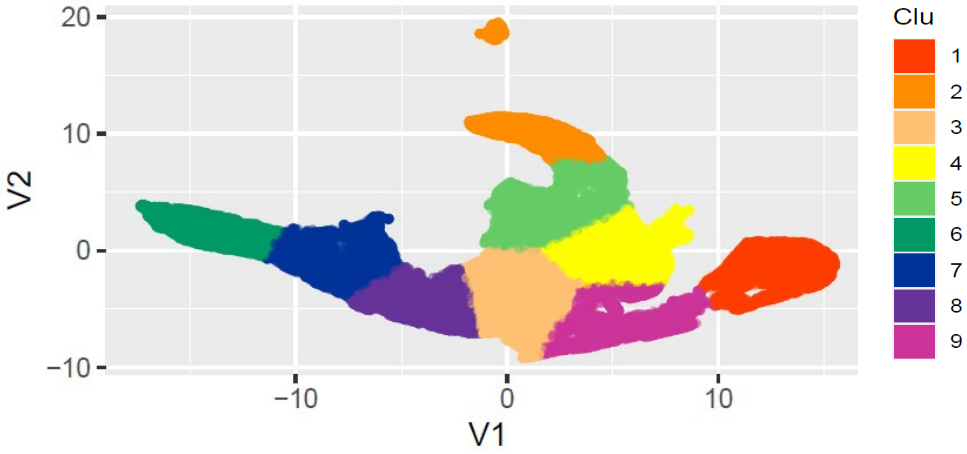
Clu
1
2
3
4
5
6
7
8
9
V2
20
10
0
−10
−10
0
10
V1

Table1 Spearman correlation of an unknown with ratio and non-ratio entities

Entity	Unknown [M-H] 375 23059
CPA 18:1	0 86090633
CPA 16:0	0 85862853
Docosahexaenoic_Acid	0 84761078
Palmitic_Acid	0 80091519
LPA 18:1	0 78455912
LPA 16:0	0 77663768
Oleic_Acid	0 77371792
PA 34:2	0 73231961
PA 36:3	0 72919804
Palmitoleic_Acid	0 72724047
CPA 18:0	0 70128825
LPE 16:0	0 69156441
PA 38:6	0 68799022
LPA 18:0	0 67264794
558. 4283	0 67163649
PE P 16:0	0 66456185
Linoleic_Acid	0 65773742
PI 36:2	0 65460109
LPA 18:2 / LPA 18:1	-0 53780801
PA 36:1 / LPA 18:1	-0 4549225
PA 36:4 / LPA 16:0	-0 42353603

Table 2 Brain glutamate to glutamine ratio positively correlates $FeCl_2$ using combined ratio and non-ratio pixel data and spearman correlation

Metabolite or Metabolite ratio	Gltamate / Glutamine
Glutamate / Glutamine	1
N-Acetylaspartate / Glutamine	0.69140746
Glutamate / Glucose	0.68318508
Aspartiate / Glutamine	0.617246741
Aspartate / Glucose	0.571634522
N-Acetylaspartate / Glucose	0.487447557
Glutathione / Glutamine	0.482704981
Glutamate / Malate	0.477826203
Glutamate / NAAG	0.418208761
Glutathione / Glucose	0.414914055
Glutamate / Taurine	0.408270132
Aspartate / NAAG	0.40560898
$FeCl_2$	0.40137113

Table S1 Brain glutamine to glutamate ratio negatively correlates $FeCl_2$ using combined ratio and non-ratio pixel data and spearman correlation

Metabolte or Metabolite ratio	Glutamine /Glutamate
Glutamine / Glutamate	1
NAA / Glutamine	-0.691412587
Glutamate / Glucose	-0.683182994
Aspartate / Glutamine	-0.617245759
Aspartate / Glucose	-0.571635589
NAA / Glucose	-0.48745363
Glutathione / Glutamine	-0.482699341
Glutamate / Malate	-0.477828273
Glutamate / NAAG	-0.418214673
Glutathione / Glucose	-0.414916374
Glutamate / Taurine	-0.408268788
Aspartate / NAAG	-0.40561461
$FeCl_2$	-0.40137478

Table S2 list of glutamate metabolism related metabolites for ratio generation and PCA segmentation of brain sections

m/z	Name
215.03279	Glucose+Cl
191.01973	Citrate
133.01425	Malate
132.03023	Aspartate
146.04588	Glutamate
145.06187	Glutamine
174.0408	N-Acetylaspartate
303.08339	N-Acetylaspartylglutamate
124.00739	Taurine
306.07653	Glutathione

Table S3 list of lyso PEs for ratio generation and PCA segmentation of brain sections

m/z	Name
478.2939	LPE 18:1
506.3252	LPE 20:1
500.2782	LPE 20:4
528.3095	LPE 22:4
524.2782	LPE 22:6

Table S4 Comparing correlation of neurotransmitter related metabolites and ratios in ROI7 of WT and KO brains

Entity Name	Spearman R square (WT)	Spearman R square (KO)
Glutamate/Glutamine	1	1
Glutamate/Glucose	0.852795869	0.678393963
Glutamate/Aspartic acid	0.801507737	0.558480678
Glutamate/N_Acetylaspartylglutamate	0.800125626	0.597592592
N_Acetylaspartate/N_Acetylaspartylglutamate	0.759938917	0.543231796
Taurine/N_Acetylaspartylglutamate	0.747279077	0.493250032
GSH/N_Acetylaspartylglutamate	0.725654702	0.534683985
Citrate/N_Acetylaspartylglutamate	0.670060429	0.3079266
Aspartate/N_Acetylaspartylglutamate	0.659178165	0.568779025
Glutamate/Malic acid	0.65035649	0.666255195
Taurine/Glutamine	0.648921859	0.554419257
Taurine/Glucose	0.644297546	0.452028615
Glutamine/N_Acetylaspartylglutamate	0.643225848	0.436576981
Malate/N_Acetylaspartylglutamate	0.624522126	0.441813603
Glutamate/N-Acetylaspartate	0.603496857	0.536109488
Glutamate/GSH	0.592151602	0.531586301
Taurine/GSH	0.567926578	0.282270798
Taurine/Malic acid	0.561595842	0.437632948
Glucose/N_Acetylaspartylglutamate	0.546762829	0.456179028
Taurine/Aspartate	0.543991912	0.289845889
N-Acetylaspartate/Glucose	0.485692311	0.460863975
Adenosine	0.48250312	0.339646908
Taurine/N-Acetylaspartate	0.480117014	0.263254553
Taurine/Citrate	0.444918698	0.56298861
Glutamine/Glucose	0.431762837	0.252386832
Glutamate	0.427270886	0.528188618
Glutamate/Citrate	0.414241714	0.592641696
Docosahexaenoic acid/Oleic acid	0.412424989	0.316780465
GSH/Glucose	0.409754542	0.418037354
N-Acetylaspartate/Glutamine	0.402130321	0.503623165
Glutamine/N-Acetylaspartate	-0.402121379	-0.503623105
Glucose/GSH	-0.409720091	-0.418038021
Oleic acid/Docosahexaenoic acid	-0.412418152	-0.316772044
Citrate/Glutamate	-0.41420686	-0.592642619
Glucose	-0.414832304	-0.247192996
Glucose/Glutamine	-0.431769617	-0.252433325
Cytidine	-0.440811865	-0.091933842
Citrate/Taurine	-0.444846276	-0.562985142
Glycerylphosphorylethanolamine	-0.446969716	-0.132695491
N-Acetylaspartate/Taurine	-0.480131641	-0.263259877
Glucose/Acetylaspartate	-0.485566843	-0.460873356
Aspartate/Taurine	-0.543994549	-0.2898528
N_Acetylaspartylglutamate//Glucose	-0.546773877	-0.456197823
Ribothymidine	-0.553276958	-0.345023745
Hypoxanthine	-0.55899857	-0.220084088
Threonate	-0.559486345	-0.21885935
Malate/Taurine	-0.56159942	-0.437638439
GSH/Taurine	-0.56793975	-0.28227912
Glutamyl_L_hydroxyproline	-0.576156273	-0.366588722
GSH/Glutamate	-0.592167807	-0.531584116
N-Acetylaspartate/Glutamate	-0.603520459	-0.536111131
N_Acetylaspartylglutamate/Malic acid	-0.624526454	-0.441825388
N_Acetylaspartylglutamate/Glutamine	-0.643220125	-0.43659667
Glucose/Taurine	-0.644270344	-0.452036941
Glutamine/Taurine	-0.64890671	-0.554426135
Malate/Glutamate	-0.650339314	-0.666263387
Inosine	-0.652470417	-0.328246954
N_Acetylaspartylglutamate	**-0.657380577**	**-0.463920793**
N_Acetylaspartylglutamate/Aspartic acid	**-0.659182447**	**-0.568791965**
N_Acetylaspartylglutamate/Citrate	-0.670054261	-0.307934844
N_Acetylaspartylglutamate/GSH	-0.725656919	-0.53469776
N_Acetylaspartylglutamate/Taurine	-0.747279393	-0.493256641
N_Acetylaspartylglutamate/N-Acetylaspartate	**-0.759938281**	**-0.543230626**
N_Acetylaspartylglutamate/Glutamate	-0.800114153	-0.59760264
Aspartate/Glutamate	-0.80148754	-0.55847547
Glucose/Glutamate	-0.852793526	-0.678396625
Glutamine/Glutamate	-0.999998899	-0.999999747